CMOS-MEMS Downconversion Mixer-Filters

by

UMUT ARSLAN

A thesis submitted in partial fulfillment of the requirements
for the
degree of

Master of Science

December 2005

Department of Electrical & Computer Engineering
Carnegie Mellon University
Pittsburgh, Pennsylvania, USA

Advisor: Dr. Tamal Mukherjee
Second Reader: Professor Gary K. Fedder

Report Documentation Page

Form Approved
OMB No. 0704-0188

Public reporting burden for the collection of information is estimated to average 1 hour per response, including the time for reviewing instructions, searching existing data sources, gathering and maintaining the data needed, and completing and reviewing the collection of information. Send comments regarding this burden estimate or any other aspect of this collection of information, including suggestions for reducing this burden, to Washington Headquarters Services, Directorate for Information Operations and Reports, 1215 Jefferson Davis Highway, Suite 1204, Arlington VA 22202-4302. Respondents should be aware that notwithstanding any other provision of law, no person shall be subject to a penalty for failing to comply with a collection of information if it does not display a currently valid OMB control number.

1. REPORT DATE	2. REPORT TYPE	3. DATES COVERED
DEC 2005		**00-00-2005 to 00-00-2005**

4. TITLE AND SUBTITLE	5a. CONTRACT NUMBER
CMOS-MEMS Downconversion Mixer-Filters	5b. GRANT NUMBER
	5c. PROGRAM ELEMENT NUMBER
6. AUTHOR(S)	5d. PROJECT NUMBER
	5e. TASK NUMBER
	5f. WORK UNIT NUMBER
7. PERFORMING ORGANIZATION NAME(S) AND ADDRESS(ES) **Carnegie Mellon University,Department of Electrical and Computer Engineering,Pittsburgh,PA,15213-3890**	8. PERFORMING ORGANIZATION REPORT NUMBER
9. SPONSORING/MONITORING AGENCY NAME(S) AND ADDRESS(ES)	10. SPONSOR/MONITOR'S ACRONYM(S)
	11. SPONSOR/MONITOR'S REPORT NUMBER(S)

12. DISTRIBUTION/AVAILABILITY STATEMENT
Approved for public release; distribution unlimited

13. SUPPLEMENTARY NOTES

14. ABSTRACT
see report

15. SUBJECT TERMS

16. SECURITY CLASSIFICATION OF:			17. LIMITATION OF ABSTRACT	18. NUMBER OF PAGES	19a. NAME OF RESPONSIBLE PERSON
a. REPORT	b. ABSTRACT	c. THIS PAGE			
unclassified	**unclassified**	**unclassified**	**Same as Report (SAR)**	**60**	

Standard Form 298 (Rev. 8-98)
Prescribed by ANSI Std Z39-18

Abstract

The potential use of CMOS-MEMS downconversion mixer-filters in future reconfigurable integrated radios is demonstrated. Analytical and simulation models have been developed to enable mixer-filter design. An array of cantilever mixer-filters is designed and fabricated. The tested mixer-filter has a center frequency of 1.05 MHz, bandwidth of 1.3 kHz and a conversion-insertion loss of 72 dB, which are in good agreement with the analytical and simulated results. The simulated noise figure is 85 dB while the IIP3 voltage is calculated as 88 dBV. The design space has been explored showing that the loss can be reduced below 10 dB with the use of 0.2 μm gaps and <30 fF load capacitance. However, the noise figure with values higher than 50 dB seems to be a major concern. The mixer-filter naturally exhibits IM2 distortion, which may be rejected using differential LO topologies, and has a superior IM3 performance.

Acknowledgement

First of all, I would like to thank my advisor Dr. Tamal Mukherjee for his constant guidance and encouragement during the course of this work. He also reviewed this report and his feedback led to significant improvements in a very short time. I would also like to thank Prof. Gary K. Fedder for his insightful comments and taking out his time from his busy schedule to read my thesis.

I would like to thank all my MEMS lab colleagues for their support. Fang Chen deserves special thanks for helping me with the post-processing and testing of my chips. I would also like to thank Suresh Santhanam for providing the vacuum system support, Sarah Bedair and Peter Gilgunn for doing the post-processing of my chips, and Chiung-C. Lo for his patience with the wirebonder. I have learnt a lot from the discussions with my colleagues - Altug Oz, Abhishek Jajoo, Hasan Akyol, Chiung-C. Lo, Ryan Magargle and Gokce Keskin - and would like to thank them.

Finally, I would like to thank my parents, sister, relatives, and friends for their love and moral support throughout the course of this work.

This work was funded by the DARPA/MTO NMASP program under award DAAB07-02-CK001.

Table of Contents

Abstract i

Acknowledgement ii

Table of Contents iii

List of Figures v

Chapter 1 Introduction 1

1.1 MEMS Mixer-Filter 2

1.2 MEMS Channel Selectable Architecture 3

1.3 Computer Aided Design (CAD) using NODAS 4

1.4 CMOS-MEMS Micromachining 5

1.5 Thesis Outline 6

Chapter 2 Analysis of CMOS-MEMS Mixer-Filters 7

2.1 Mixer-Filter Operation 7

2.1.1 Electrostatic Actuation 7

2.1.2 Mechanical Resonance 10

2.1.3 Electrostatic Sensing 12

2.1.4 Correction Terms 15

2.1.4.1 Feedback Currents and Forces 15

2.1.4.2 Capacitor Nonlinearity 16

2.2 Mixer-Filter Design Specifications 17

2.2.1 Center Frequency and Bandwidth 18

2.2.2 Conversion-Insertion Gain 20

2.2.3 Noise Figure (NF) 21

2.2.4 Linearity 23

2.3 Image Rejection 25

Chapter 3 Computer Aided Design of CMOS-MEMS Mixer-Filters 27

3.1 NODAS Cantilever Resonator Model 27

3.2 Preamplifier 29

3.3 Differential Mixer-Filter Topology 30

3.4 Mixer-Filter Array Layout 30

3.5 Simulations 32

3.5.1 Mixer-filter Testbench 33

3.5.2 System Testbench 33

Chapter 4 Results 36

4.1 PCB Design and Characterization 36

4.2 Measured Results 37

4.2.1 Resonator Characteristics 39

4.2.2 Mixer-Filter Characteristics 40

4.3 Specifications vs. Design Parameters 42

4.3.1 Resonant (Center) Frequency 43

4.3.2 Conversion-Insertion Gain 44

4.3.3 Noise Figure 45

4.3.4 Linearity 46

4.3.5 Discussion on Effective Damping 46

Chapter 5 Conclusions 48

Bibliography 49

Appendix: Feedback Forces 51

List of Figures

Figure 1-1 The superheterodyne receiver. 2

Figure 1-2 MEMS channel-selectable architecture. 3

Figure 1-3 Cross-section of CMOS-MEMS micromachining process: (a) After foundry CMOS processing, (b) after anisotropic dielectric etch, (c) after final release using a combination of anisotropic silicon DRIE and isotropic silicon etch. 5

Figure 2-1 Cantilever resonator with hollow square head. 7

Figure 2-2 Electrostatic actuation. 8

Figure 2-3 Normalized force magnitudes vs. frequency. 10

Figure 2-4 Mechanical resonance. 11

Figure 2-5 Electrostatic sensing. 12

Figure 2-6 Second-order intermodulation (IM2) products due to the quadratic force relation. 23

Figure 2-7 An example of IM2-reject mixer-filter. 24

Figure 2-8 An example of IM2 + image reject mixer-filter. 26

Figure 3-1 The cantilever mixer-filter: (a) Illustration (b) NODAS model. 28

Figure 3-2 Preamplifier schematic with W/L ratios (a) Differential amplifier with source follower output stages (b) Biasing stage. 29

Figure 3-3 Differential Mixer-Filter. 31

Figure 3-4 (a) Complete layout (b) Grounded shield between RF/LO and DC+/DC-. .. 32

Figure 3-5 Mixer-filter testbench. 33

Figure 3-6 Schematic system testbench. 34

Figure 3-7 Extracted system testbench. 35

Figure 4-1 (a) PCB with chip wirebonded (b) Vacuum chamber capable of sub-1m Torr.36

Figure 4-2 (a) PCB Traxmaker schematic with highlighted RF and LO traces (b) Measured S11 for RF and LO ports. 37

Figure 4-3 (a) Direct-drive test setup (b) Mixing test setup. 38

Figure 4-4 Resonator frequency characteristics under 100 mTorr pressure with VDCin = VDCout+ = VDCout- = 10V. 39

Figure 4-5 Measured system response under 100 mTorr vacuum with VDCin = VDCout+ = 10V, and VDCout- = Vbias = 1.65 V. 40

Figure 4-6 (a) Measured system gain for fLO stepped from 100 to 300 MHz with VLO = 1.4 V, VDCout+ = 10 V, VDCout- = Vbias = 1.65 V. (b) Gain distribution between the system blocks. 41

Figure 4-7 Resonant frequency (a) vs. gap for VLO = 1 V, ΔVDCin = 0 V, ΔVDCout = 8 V and Cp = 150 fF, (b) vs. VLO for gap = 0.2 μm, ΔVDCin = 0 V, ΔVDCout = 8 V and Cp = 150 fF, (c) vs. ΔVDCout for gap = 0.2 μm, VLO = 1 V, ΔVDCin = 0 V, and Cp = 150 fF, (d) vs. Cp for gap = 0.2 μm, VLO = 1 V, ΔVDCin = 0 V, and ΔVDCout = 8 V. 43

Figure 4-8 Conversion-insertion gain (a) vs. gap for VLO = 1 V, ΔVDCin = 0 V, ΔVDCout = 8 V and Cp = 150 fF, (b) vs. VLO for gap = 0.2 μm, ΔVDCin = 0 V, ΔVDCout = 8 V and Cp = 150 fF, (c) vs. ΔVDCout for gap = 0.2 μm, VLO = 1 V, ΔVDCin = 0 V, and Cp = 150 fF, (d) vs. Cp for gap = 0.2 μm, VLO = 1 V, ΔVDCin = 0 V, and ΔVDCout = 8 V. 44

Figure 4-9 NF (a) vs. gap for VLO = 1 V and RsRF = 50 Ω, (b) vs. VLO for gap = 0.2 μm and RsRF = 50 Ω, (c) vs. RsRF for gap = 0.2 μm and VLO = 1 V. 45

Figure 4-10 IIP3 voltage (a) vs. input gap for f0 = 1 MHz, fLO = 100 MHz, VLO = 1 V, and ΔVDCin = ΔVDCout = 10 V, (b) vs. ΔVDCin for f0 = 1 MHz, fLO = 100 MHz,

VLO = 1 V, gapin = 0.2 μm, VLO = 1 V, and ΔVDCout = ΔVDCin. 46

Figure A.1 Feedback forces at (a) input and (b) output nodes. 51

1 Introduction

Modern wireless communication systems use radio-frequency (RF) signals, with frequencies in the range of hundreds of megahertz (MHz) to several gigahertz (GHz), for the transmission and reception of information through the air. Both the transmitters and receivers comprise RF front-ends that interfaces with the air. The information signal, which is usually at low frequencies, is modulated into an RF signal and sent into the air by the transmitter front-end. The received signal is demodulated to obtain the information signal by the receiver front-end. Both front-ends employ active circuits (amplifiers, mixers, oscillators, etc.) and passive networks (matching networks, filters, etc.) for the essential signal processing [1]. One of the major trends in modern RF design is the integration of all these blocks on a single silicon substrate to produce low-cost, low-power, miniature radios. With the tremendous progress in integrated-circuit (IC) technologies, most of the active circuits have been integrated on silicon substrate. However, performance requirements have prevented full-integration of filters.

Modern wireless communications comprise multiple radio standards (GSM, IS-95, etc.) and each standard can only make use of a limited frequency band in the whole radio spectrum. Furthermore, a standard usually allocates a small portion of its band, which is called a channel, to each user in order to share the available band between multiple users. Thus, a receiver front-end has to filter the spectrum at its input only passing the assigned channel. However, filtering kHz-wide channels centered at GHz frequencies requires prohibitively high quality-factor (Q) filters. The superheterodyne receiver, which was invented to relax the Q requirement, first filters the band, amplifies and downconverts it to an intermediate frequency (IF) and then filters it at the IF for channel selection (Figure 1-1). Although the required Q is reduced, it is still far from being attainable by integrated passives (i.e. inductors and capacitors). Hence, the superhetero-

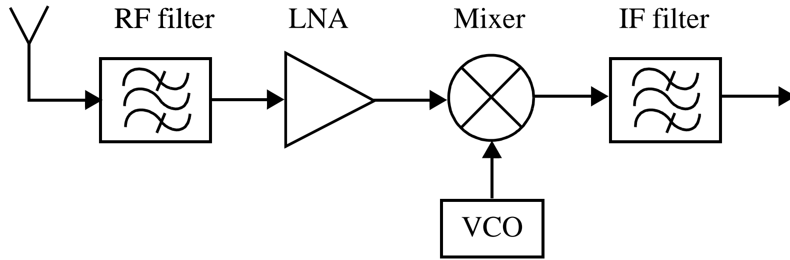

Figure 1-1 The superheterodyne receiver.

dyne receivers have been filtering both the RF (i.e. band) and the IF (i.e. channel) off-chip using ceramic, quartz crystal, SAW (Surface acoustic wave), and recently FBAR (Film Bulk Acoustic Resonator) filters, capable of achieving *Q*'s from 500 to 10000. Off-chip filtering prevents the miniaturization, low-cost production and low-power operation of the receivers.

1.1 MEMS Mixer-Filter

With the advent of the MEMS technology, micromechanical filters were proposed as having potential for the signal processing applications that require high *Q* [2]. Their manufacturability by IC-compatible processes have promised the full-integration of RF-front ends. The pursuit of building a MEMS RF channel-select filter has directed the recent research to maximize both the *Q* and the resonant frequency of micromechanical resonators. Disk resonators with $Q \sim 156000$ at 60 MHz resonance, and frequencies of 1.5 GHz with $Q \sim 11555$ have been demonstrated [3]. Micromechanical resonators have also been coupled mechanically [4] or electrostatically [5] for higher order filtering, although at lower frequencies.

It has recently been demonstrated that micromechanical resonators can also be utilized as mixer-filters, and thus eliminate the need for channel filtering at GHz while retaining the benefits of high mechanical *Q* [6] [7]. MEMS mixer-filters exploit the nonlinearity of the electrostatic force with the drive voltage in the electromechanical resonators, downconverting GHz RF input signals to excite MHz mechanical resonance for IF filtering. Mechanical displacement is then capacitively transduced into an electrical IF output. In essence, mixing and filtering functions are achieved simultaneously as the RF signals pass through the resonators.

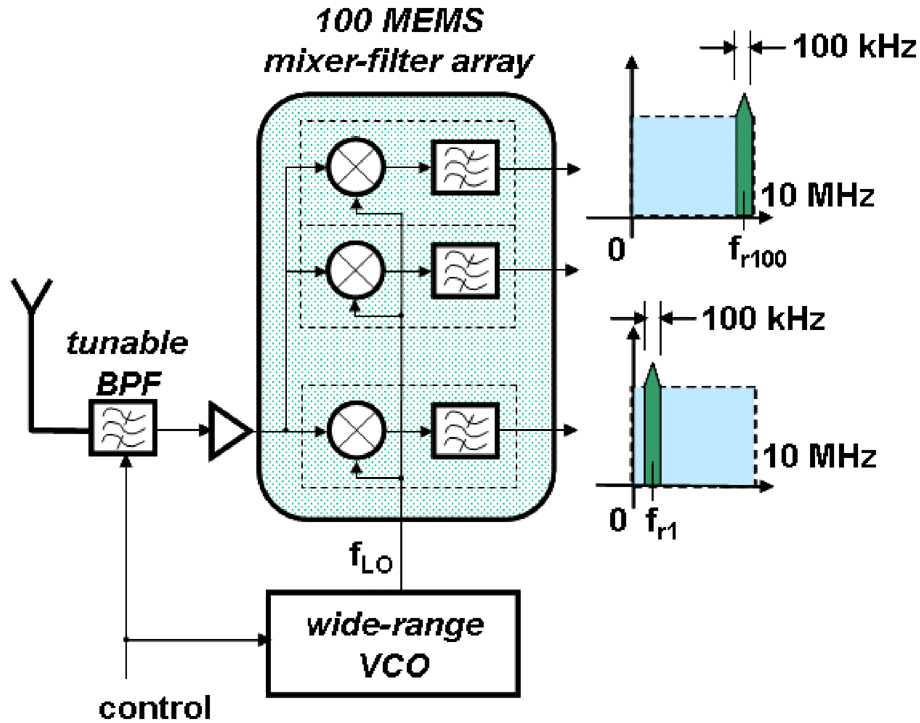

Figure 1-2 MEMS channel-selectable architecture.

Design of a MEMS mixer-filter necessitates a solid understanding of its operation principles. Therefore, this thesis analyzes the mixer-filter operation and the design specifications - center frequency and bandwidth, conversion-insertion gain, noise figure, linearity - that determine its performance.

1.2 MEMS Channel Selectable Architecture

In addition to the integration trend in the market, there is also an increasing demand for reconfigurable multi-band radios that can work with multiple wireless standards. Although software reconfiguration is the ultimate goal in multi-band radios, power and dynamic range limitations require some of the reconfiguration to take place in the RF front-end [8]. With the advantages of high Q, low power and small size, MEMS mixer filters have the potential to be key components in future reconfigurable multi-band single-chip radios. However, a MEMS mixer-filter is not widely tunable and hence the reconfiguration is a challenge. To overcome this challenge, we use an array of parallel mixer-filters each having a unique center frequency and electrically select one of the mixer-filter outputs. Figure 1-2. shows a strawman channel-

selectable architecture in which a mixer-filter array of size 100 can select 100 kHz wide channels and span the frequency range from about DC to 10 MHz. When the array is driven by a wide-range tunable VCO (voltage-controlled oscillator) that is hopping 10 MHz, the system can span a wider frequency range (e.g. 100 MHz), which has to be first filtered by a front-end tunable BPF (bandpass filter). Essentially, the whole wireless spectrum of interest (i.e. 100 MHz to 10 GHz) can be spanned with such a two-level reconfigurable radio architecture.

Building an array of MEMS mixer-filters and integrating it with the neighboring circuits require a good understanding of individual mixer-filter performance. Thus, this work tries to construct this understanding in order to design mixer-filter arrays with admissible performance.

1.3 Computer Aided Design (CAD) using NODAS

MEMS mixer-filter design optimization, very similar to electrical circuit design optimization, necessitates CAD tools. Therefore, we need an accurate resonator model and a simulation environment that offers MEMS-IC co-simulation together with fast and accurate RF analyses.

NODAS, a set of lumped element electromechanical models developed at Carnegie Mellon University [9], gives us the capability to build a resonator model from the atomic elements: beams, plates and gaps. NODAS uses the Verilog-A hardware modeling language and can be simulated using Cadence Spectre and SpectreRF simulators. Due to its compatibility with the IC design tools, NODAS also enables parasitic layout extraction, which is crucial in high-frequency design.

This thesis describes the NODAS modeling and simulation of a cantilever mixer-filter. It compares the simulation results with the analytical and measured results to verify our understanding. It also discusses the necessity of NODAS simulations for design optimization.

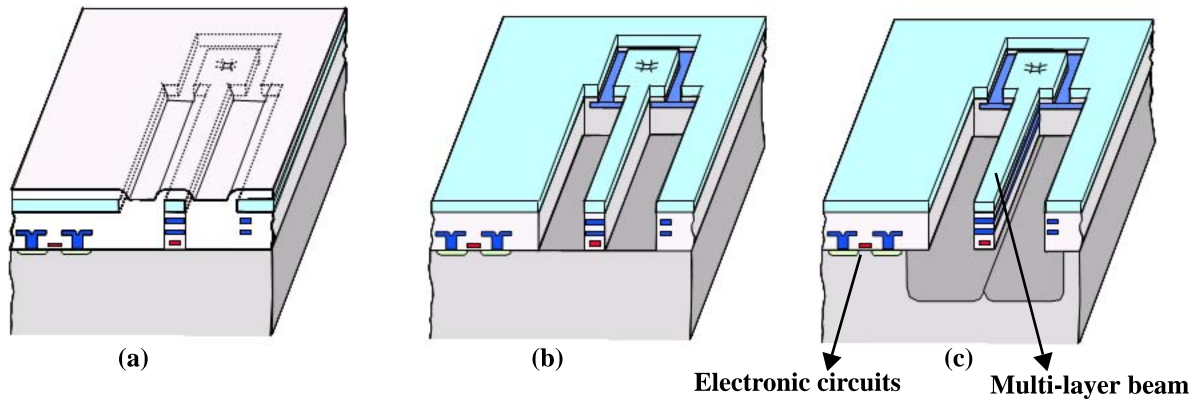

Figure 1-3 Cross-section of CMOS-MEMS micromachining process: **(a)** After foundry CMOS processing, **(b)** after anisotropic dielectric etch, **(c)** after final release using a combination of anisotropic silicon DRIE and isotropic silicon etch.

1.4 CMOS-MEMS Micromachining

The CMOS-MEMS process that was developed at Carnegie Mellon University [10] starts with a foundry-fabricated four-metal CMOS chip with cross-section shown in Fig. 1-3a. MEMS structures are micromachined through a sequence of dry etch steps. First, a CHF_3:0_2 reactive-ion etch (RIE) removes any dielectric that is not covered with metal (Fig. 1-3b). The top metal layer is used to protect the electronic circuits that reside alongside the MEMS structures. Second, an anisotropic etch of the exposed silicon substrate using the Bosch deep-reactive-ion etch (DRIE) sets the spacing from the microstructures to the substrate. A subsequent isotropic etch of silicon in an SF_6 plasma undercuts and releases the MEMS structures. The released structure is a stack of metal and oxide layers such as the beam shown in Fig. 1-3c.

CMOS-MEMS offers several advantages for the fabrication of mixer-filters. First of all, it allows us to build radios by integrating MEMS with electronics on the same substrate. The embedded aluminum interconnects inside the microstructures enables mixer-filter design with multiple isolated electrodes that improve the device functionality and minimize the feedthrough between the nodes. The metal interconnects also provide low resistance and thereby less attenuation for the RF signals. Besides, better system performances are achievable with the benefit of short (i.e. low-capacitance) interconnects between the MEMS and integrated circuits [11].

An array of MEMS mixer-filters were designed and fabricated using CMOS-MEMS micromachining. The mixer-filter with a resonant frequency of ~1 MHz was tested and the measured data was compared with the analytical and simulated results.

1.5 Thesis Outline

Chapter 2 builds an analytical model for a cantilever mixer-filter by formulating its principles of operation and design specifications. Chapter 3 describes the computer aided design and simulation of mixer-filters using NODAS. Chapter 4 explains the characterization of mixer-filters, demonstrates the measured data for a ~1 MHz cantilever mixer-filter and compares it with the analytical and simulated results. It also explores the design space in the pursuit of an optimized device performance. Chapter 5 concludes the thesis by discussing the achievements, challenges and the possible solutions.

2 Analysis of CMOS-MEMS Mixer-Filters

2.1 Mixer-Filter Operation

The MEMS channel-selectable architecture (Figure 1-2) is essentially a low-IF radio, and thus bending-mode resonators, which typically resonate in the kHz-MHz range, may be utilized as mixer-filters. The previous work on CMOS-MEMS resonators encouraged the use of cantilevers (Figure 2-1), by demonstrating that they are more robust to variations in compressive residual stress in the CMOS stack when compared to fixed-fixed resonators [12][13]. The cantilever focused in this work is anchored at one end and has a square frame at the tip to separate the RF and output nodes in order to reduce feedthrough. We will start by explaining its operation principles.

2.1.1 Electrostatic Actuation

As illustrated in Figure 2-2, a variable parallel-plate capacitor (i.e. an electromechanical transducer) is formed by placing an anchored electrode across the resonator electrode. Applying a time-varying voltage difference, ΔV_{in}, across this variable capacitor, C_{in}, generates an input electrostatic force, F_{in}, given by

$$F_{in}(t) = \frac{1}{2}\frac{\partial C_{in}}{\partial x}\Delta V_{in}(t)^2 . \qquad (2.1)$$

Taking the derivative of the instantaneous capacitance, $C_{in}(t) = \varepsilon_0 A_{in}/[g_{in} + x(t)]$, we get

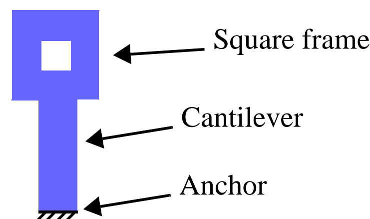

Figure 2-1 Cantilever resonator with hollow square head.

$$\frac{\partial C_{in}}{\partial x} = -\frac{\varepsilon_0 A_{in}}{[g_{in} + x(t)]^2} \tag{2.2}$$

where ε_0 is the permittivity of vacuum, A_{in} is the electrode area, g_{in} is the nominal gap and $x(t)$ is the instantaneous displacement.

For sufficiently large nominal gaps and small forces, the displacement is much smaller than the gap ($|x(t)| << g_{in}$), and thus $\frac{\partial C_{in}}{\partial x}$ can be approximated as a constant whose value is determined by the capacitor dimensions. Doing so yields

$$\frac{\partial C_{in}}{\partial x} \approx -\frac{\varepsilon_0 A_{in}}{g_{in}^2} = -\frac{C_{0in}}{g_{in}} \tag{2.3}$$

where C_{0in} is the nominal input capacitance.

The nonlinearity of the electrostatic force with voltage is capable of mixing two signals. Here, we apply the RF signal to the anchored electrode and the LO to the resonator electrode as shown in Figure 2-2. Both signals may also have DC offsets, denoted by V_{DCrf} and V_{DClo}, causing ΔV_{in} to have a DC term, which will be denoted by ΔV_{DCin} for convenience ($\Delta V_{DCin} = V_{DCrf} - V_{DClo}$). Hence, inserting $\Delta V_{in}(t) = v_{RF}(t) - v_{LO}(t) + \Delta V_{DCin}$ together with (2.3) into (2.1) gives:

$$F_{in}(t) = -\frac{\varepsilon_0 A_{in}}{2 g_{in}^2}[v_{RF}(t) - v_{LO}(t) + \Delta V_{DCin}]^2 \tag{2.4}$$

where $v_{RF}(t) = V_{RF}cos(\omega_{RF}t)$ and $v_{LO}(t) = V_{LO}cos(\omega_{LO}t)$.

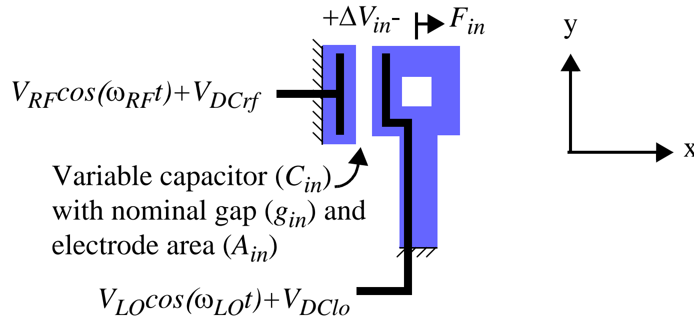

Figure 2-2 Electrostatic actuation.

Expanding the quadratic expression and transforming the terms using the basic trigonometric identities gives force components at various frequencies, which are listed in Table 2-1.

Table 2-1. Components of force at various frequencies.

Frequency (ω)	**Input force** ($F_{in}(t)$)
0	$-\frac{\varepsilon_0 A_{in}}{2g_{in}^2}\left[\frac{1}{2}(V_{RF}^2 + V_{LO}^2) + \Delta V_{DCin}^2\right]$ (2.5)
ω_{RF}	$-\frac{\varepsilon_0 A_{in}}{g_{in}^2}\Delta V_{DCin} V_{RF} cos(\omega_{RF} t)$ (2.6)
ω_{LO}	$\frac{\varepsilon_0 A_{in}}{g_{in}^2}\Delta V_{DCin} V_{LO} cos(\omega_{LO} t)$ (2.7)
ω_{RF}-ω_{LO} (= ω_{IF})	$\frac{\varepsilon_0 A_{in}}{2g_{in}^2} V_{RF} V_{LO} cos[(\omega_{RF} - \omega_{LO})t]$ (2.8)
$\omega_{RF}+\omega_{LO}$	$\frac{\varepsilon_0 A_{in}}{2g_{in}^2} V_{RF} V_{LO} cos[(\omega_{RF} + \omega_{LO})t]$ (2.9)
$2\omega_{RF}$	$-\frac{\varepsilon_0 A_{in}}{4g_{in}^2} V_{RF}^2 cos(2\omega_{RF} t)$ (2.10)
$2\omega_{LO}$	$-\frac{\varepsilon_0 A_{in}}{4g_{in}^2} V_{LO}^2 cos(2\omega_{LO} t)$ (2.11)

Figure 2-3 illustrates the normalized force magnitudes vs. frequency when $V_{RF} = V_{LO} = \Delta V_{DCin}$. For typical GHz RF and LO frequencies, the terms at $\omega_{RF}+\omega_{LO}$, $2\omega_{RF}$ and $2\omega_{LO}$ also occur at GHz. However, the term at ω_{RF}-ω_{LO}, which is called as the intermediate frequency (IF), may occur in the kHz-MHz range depending on the RF-LO frequency separation.

2.1.2 Mechanical Resonance

A micromechanical resonator acts as a spring-mass-damper system whose response is defined by the general equation of motion, given by

$$F_{in}(t) = m\ddot{x}(t) + b\dot{x}(t) + kx(t). \tag{2.12}$$

As the micromechanical resonator is an underdamped system, its displacement phasor is related to the input force phasor with the expression,

$$X(j\omega) = \frac{F_{in}(j\omega)}{k}\left[\underbrace{\frac{1}{1 + \frac{j\omega}{Q\omega_0} - \left(\frac{\omega}{\omega_0}\right)^2}}_{\Theta(j\omega)}\right] \tag{2.13}$$

where $\omega_0 = \sqrt{\frac{k}{m}}$ and $Q = \frac{k}{\omega_0 b}$ for a resonator with mass m, spring constant k and the damping coefficient b (Figure 2-4).

The frequency selectivity of a resonator is determined by its quality factor (Q) and can be exhibited by simplifying (2.13) for three different frequency regions, as shown below.

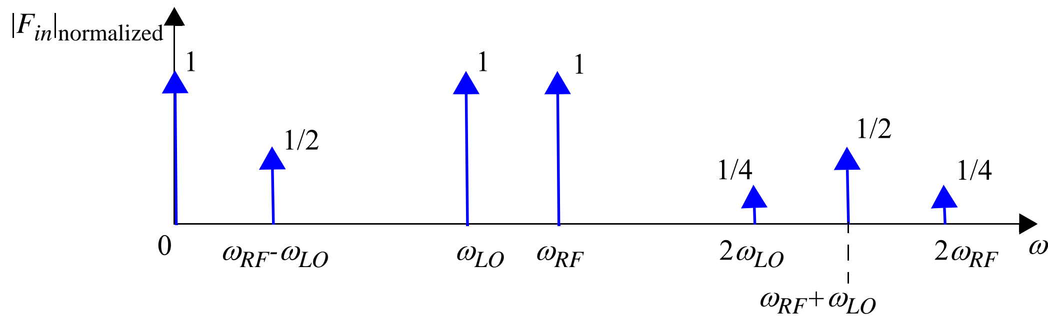

Figure 2-3 Normalized force magnitudes vs. frequency.

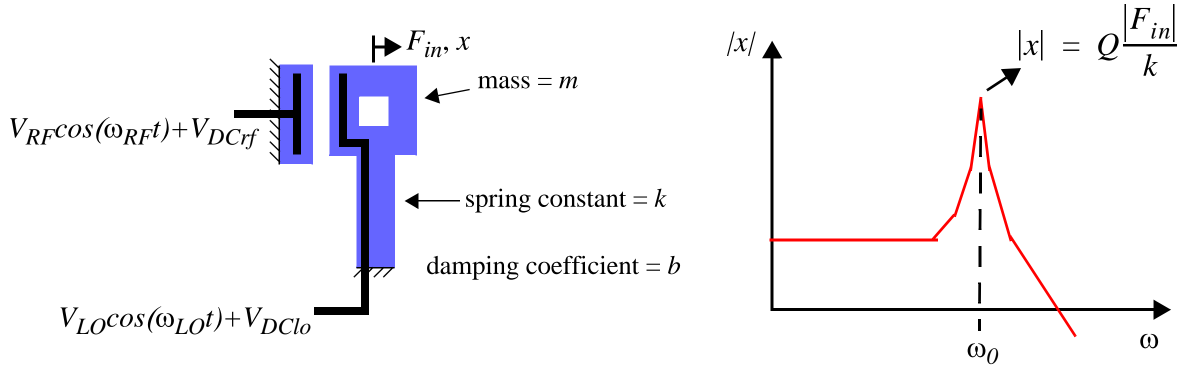

Figure 2-4 Mechanical resonance

$$X(j\omega) \approx \frac{F_{in}(j\omega)}{k} \qquad ;\omega \ll \omega_0, \tag{2.14}$$

$$X(j\omega_0) = \frac{QF_{in}(j\omega_0)}{jk} \qquad ;\omega = \omega_0, \tag{2.15}$$

$$X(j\omega) \approx -\frac{F_{in}(j\omega)}{k}\left(\frac{\omega_0}{\omega}\right)^2 \qquad ;\omega \gg \omega_0. \tag{2.16}$$

With the advantage of high Q, a micromechanical resonator can substantially filter out the input forces that have frequencies far from its resonant frequency. High Q also provides narrowband filtering, since the -3 dB bandwidth is defined by $\Delta\omega_{-3dB} = \frac{\omega_0}{Q}$. This relation also asserts that a high-ω_0 resonator requires a higher Q than its low-ω_0 counterpart in order to provide the same bandwidth. Accordingly, the MEMS-enhanced receiver architecture described in Chapter 1 relaxes the required Q by employing low-ω_0 (from DC to 10 MHz) mixer-filters. The cantilever focused in this work fits into the architecture as it typically resonates in the kHz-MHz range. For a low-ω_0 mixer-filter, the input IF force turns out to be the only force that can be used to excite mechanical resonance since the other terms occur at GHz frequencies as mentioned in the previous section. Hence, we will focus on the IF force which is already given by (2.8) as

$$F_{in}(j\omega_{IF}) = F_{inIF} = \frac{\varepsilon_0 A_{in}}{2g_{in}^2}V_{RF}V_{LO}. \tag{2.17}$$

Now, it is also beneficial to define a new term - input electromechanical coupling factor - to point out the input transducer's efficiency in converting the RF voltage to the IF force. By expressing the IF force as

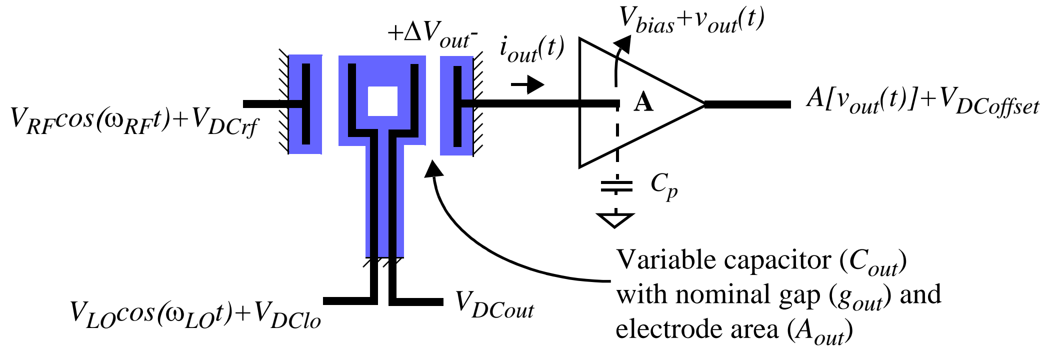

Figure 2-5 Electrostatic sensing.

$$F_{inIF} = \eta_{in} V_{RF} \tag{2.18}$$

we can define the input electromechanical coupling factor, η_{in}, by

$$\eta_{in} = \frac{\varepsilon_0 A_{in}}{2g_{in}^2} V_{LO}. \tag{2.19}$$

The resonant displacement occurs when $\omega_{IF} = \omega_0$ and is simply obtained by inserting (2.17) into (2.15). Thus, it is given by

$$X(j\omega_0) = X_0 = -j\frac{\varepsilon_0 A_{in} Q}{2g_{in}^2 k} V_{LO} V_{RF} = -j\frac{\eta_{in} Q}{k} V_{RF} \tag{2.20}$$

whose time-domain equivalent is

$$x_0(t) = -\frac{\varepsilon_0 A_{in} Q}{2g_{in}^2 k} V_{LO} V_{RF} sin(\omega_0 t). \tag{2.21}$$

2.1.3 Electrostatic Sensing

To sense the mechanical motion, a second variable parallel-plate capacitor is formed by placing an anchored electrode across the output resonator electrode as shown in Figure 2-5. Under an applied DC potential across this capacitor, the resonator displacement induces an output current, which is then converted to voltage at a load capacitor provided by an on-chip preamplifier. The output current, i_{out}, is calculated using

$$i_{out}(t) = \frac{\partial}{\partial t}(C_{out}(t)\Delta V_{out}(t)) = \Delta V_{out}(t)\frac{\partial C_{out}}{\partial x}\frac{\partial x(t)}{\partial t} + \left(C_{0out} + \frac{\partial C_{out}}{\partial x}x(t)\right)\frac{\partial \Delta V_{out}(t)}{\partial t} \quad (2.22)$$

where C_{out} is the instantaneous and C_{0out} is the nominal output capacitance. ΔV_{out} is the potential across the output gap and can be expressed in terms of the applied DC voltage, V_{DCout}, preamplifier input bias, V_{bias}, and the output potential generated by the resonator motion, v_{out}, as follows

$$\Delta V_{out}(t) = V_{DCout} - V_{bias} - v_{out}(t). \quad (2.23)$$

For small displacements (i.e. $|x(t)| << g_{out}$) and the output voltages (i.e. $|v_{out}(t)| << |V_{DCout}\text{-}V_{bias}|$), we can make the following approximations: $\Delta V_{out}(t) \approx \Delta V_{DCout} = V_{DCout} - V_{bias}$ and $C_{0out} + (\partial C_{out}/\partial x)x(t) \approx C_{0out}$. Doing so simplifies (2.22) to

$$i_{out}(t) = \Delta V_{DCout}\frac{\partial C_{out}}{\partial x}\frac{\partial x(t)}{\partial t} - C_{0out}\frac{\partial v_{out}(t)}{\partial t}. \quad (2.24)$$

Setting the currents through the transducer and load capacitors equal, we get

$$i_{out}(t) = C_p\frac{\partial v_{out}(t)}{\partial t} = \Delta V_{DCout}\frac{\partial C_{out}}{\partial x}\frac{\partial x(t)}{\partial t} - C_{0out}\frac{\partial v_{out}(t)}{\partial t}, \quad (2.25)$$

$$(C_p + C_{0out})\frac{\partial v_{out}(t)}{\partial t} = \Delta V_{DCout}\frac{\partial C_{out}}{\partial x}\frac{\partial x(t)}{\partial t}. \quad (2.26)$$

The equation above implies that the output voltage occurs at the vibration frequency. Thus, both the displacement and the output voltage is maximized at resonance. By using the approximation

$$\frac{\partial C_{out}}{\partial x} = \frac{\varepsilon_0 A_{out}}{[g_{out} - x(t)]^2} \approx \frac{\varepsilon_0 A_{out}}{g_{out}^2} \quad (2.27)$$

which is valid for $|x(t)| << g_{out}$, we relate the resonant output voltage, v_{out0}, to the resonant displacement by

$$v_{out0}(t) = \frac{\varepsilon_0 A_{out}}{g_{out}^2(C_p + C_{0out})}\Delta V_{DCout}x_0(t) \quad (2.28)$$

which can be also expressed in the frequency domain as

$$V_{out0} = \frac{\varepsilon_0 A_{out}}{g_{out}^2(C_p + C_{0out})}\Delta V_{DCout}X_0. \quad (2.29)$$

Now, we can solve for V_{out0} by inserting (2.20) into (2.29). Thus, it is given by

$$V_{out0} = -j\frac{\varepsilon_0^2 A_{in} A_{out} Q}{2g_{in}^2 g_{out}^2 k(C_p + C_{0out})} V_{LO} \Delta V_{DCout} V_{RF}. \tag{2.30}$$

Using the relation $Q = \frac{k}{\omega_0 b}$, we can rewrite the above equation as

$$V_{out0} = -j\frac{\varepsilon_0^2 A_{in} A_{out}}{2g_{in}^2 g_{out}^2 b\omega_0(C_p + C_{0out})} V_{LO} \Delta V_{DCout} V_{RF}. \tag{2.31}$$

It is also helpful to go one step back and relate the resonant output current phasor, I_{out0}, to the displacement phasor using the relations (2.25) and (2.29). Doing so yields

$$I_{out0} = j\frac{\varepsilon_0 A_{out} C_p}{g_{out}^2 (C_p + C_{0out})} \Delta V_{DCout} X_0. \tag{2.32}$$

From this relation, we can derive the output electromechanical coupling factor, η_{out}, which determines the output transducer's efficiency in converting mechanical motion to current, and it is given by

$$\eta_{out} = \frac{\varepsilon_0 A_{out} C_p}{g_{out}^2 (C_p + C_{0out})} \Delta V_{DCout}. \tag{2.33}$$

Now, the resonant output voltage can be simply written in terms of the input and output coupling factors (η_{in} and η_{out}), the mechanical damping coefficient (b), the load capacitance (C_p) and the input RF amplitude (V_{RF}):

$$V_{out0} = -j\eta_{in}\eta_{out}\frac{1}{b\omega_0 C_p} V_{RF} \tag{2.34}$$

The frequency domain analysis of the mixer-filter operation has also shown that phase shifts occur through the transduction steps. Thus, it may provide further insight to show those phase shifts with a diagram as shown below.

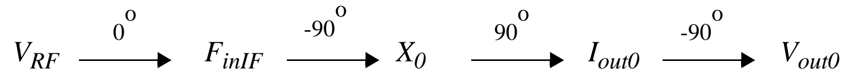

2.1.4 Correction Terms

The analysis above has entailed some simplifying assumptions to exhibit the fundamentals of mixer-filter operation. We have assumed that the input force is the only force acting on the resonator and the transducer capacitors are linear. However, to put forward a more accurate analytical model, these assumptions need to be relaxed and the analysis has to be elaborated by including some correction terms.

2.1.4.1 Feedback Currents and Forces

The input force has been assumed to be the net force exerted on the resonator. However, the resonator motion induces currents that are converted to voltages due to the finite source and load impedances (e.g. output current conversion to output voltage as explained in Section 2.1.3). The nonlinearity of the force with voltage mixes the feedback and input voltages generating force components at the mixed frequencies. Out of various force components, we need to consider only those that occur at the IF as the high-frequency forces are substantially filtered out. The detailed analysis given in Appendix shows that the feedback forces can be expressed in terms of displacement and its derivatives. Including these feedback forces, the net IF force exerted on the resonator, F_{netIF}, is given by

$$F_{netIF}(t) = F_{inIF}'(t) + F_{outIF}'(t) \tag{2.35}$$

where the IF force at the input, F_{inIF}', is

$$F_{inIF}'(t) = F_{inIF}(t) - \frac{\varepsilon_0^2 A_{in}^2 (R_{sRF} + R_{sLO})}{g_{in}^4} \left(\frac{\omega_{RF}}{4\omega_{IF}} V_{LO}^2 + \Delta V_{DCin}^2 \right) \frac{\partial x(t)}{\partial t}, \tag{2.36}$$

and at the output, F_{outIF}', is

$$F_{outIF}'(t) = -\frac{\varepsilon_0^2 A_{out}^2}{g_{out}^4 (C_p + C_{0out})} \Delta V_{DCout}^2 x(t). \tag{2.37}$$

It can be concluded by inserting F_{netIF} into the equation of motion (2.12) that the x-dependent force terms act like spring forces while the $\partial x / \partial t$-dependent terms act like damping forces. Thus, we can define an effective damping coefficient and a spring constant that include both mechanical and electrical parameters. Doing so yields the effective spring constant, k_{eff}, as

$$k_{eff} = k_{mech} + \underbrace{\frac{\varepsilon_0^2 A_{out}^2}{g_{out}^4 (C_{0out} + C_p)} \Delta V_{DCout}{}^2}_{k_{e,fb}} . \tag{2.38}$$

Considering that the damping has significance only at resonance, where $\omega_{IF} = \omega_0$, the effective damping coefficient, b_{eff}, can be given by

$$b_{eff} = b_{mech} + \underbrace{\frac{\varepsilon_0^2 A_{in}^2 (R_{sRF} + R_{sLO})}{g_{in}^4} \left(\frac{\omega_{RF}}{4\omega_0} V_{LO}^2 + \Delta V_{DCin}{}^2 \right)}_{b_{e,fb}} . \tag{2.39}$$

The analysis above has shown that the source resistors damp the resonator, while the load capacitor stiffens it. Now, we can re-express the equation of motion as follows

$$F_{inIF}(t) = m\ddot{x}(t) + b_{eff}\dot{x}(t) + k_{eff}x(t) . \tag{2.40}$$

2.1.4.2 Capacitor Nonlinearity

The assumption that the transducer capacitors are linear loses its validity as the displacement to gap ratio increases. In that case, it is more appropriate to use the first-order Taylor approximations for the capacitance derivatives, given by

$$\frac{\partial C_{in}}{\partial x} = -\frac{\varepsilon_0 A_{in}}{[g_{in} + x(t)]^2} \approx -\frac{\varepsilon_0 A_{in}}{g_{in}^2} + \frac{2\varepsilon_0 A_{in}}{g_{in}^3} x(t) , \tag{2.41}$$

$$\frac{\partial C_{out}}{\partial x} = \frac{\varepsilon_0 A_{out}}{[g_{out} - x(t)]^2} \approx \frac{\varepsilon_0 A_{out}}{g_{out}^2} + \frac{2\varepsilon_0 A_{out}}{g_{out}^3} x(t) . \tag{2.42}$$

Taking the voltage across the input gap as $\Delta V_{in}(t) = V_{RF} cos(\omega_{RF} t) - V_{LO} cos(\omega_{LO} t) + \Delta V_{DCin}$ and assuming that the input capacitor is linear, we have derived the input force components at various frequencies in (2.5)-(2.11). However, relaxing the linear capacitor assumption and using (2.41) instead will give rise to an additional IF force generated by the interaction of the *x*-dependent term ($\frac{2\varepsilon_0 A_{in}}{g_{in}^3} x(t)$) with the DC term shown in parentheses in (2.5). Similarly, taking the output voltage as $\Delta V_{out}(t) = V_{DCout} - V_{bias} + V_{out} sin(\omega_{IF} t)$ and using (2.42) give rise to another additional IF force, which has to be also added to the net force. Thus, the total IF force due to the capacitor nonlinearities is given by

$$F_{nlinIF}(t) = \frac{\varepsilon_0 A_{in}}{g_{in}^3}\left(\frac{V_{RF}^2 + V_{LO}^2}{2} + \Delta V_{DCin}{}^2\right)x(t) + \frac{\varepsilon_0 A_{out}}{g_{out}^3}\left(\frac{V_{out}^2}{2} + \Delta V_{DCout}{}^2\right)x(t)\,. \tag{2.43}$$

Since downconversion mixers usually deal with small RF amplitudes, and the MEMS mixer-filter does not provide high gain - as will be explained in Section 2.2.2 -, the terms $V^2{}_{RF}$ and $V^2{}_{out}$ in parentheses can be neglected compared to the $V^2{}_{LO}$, $\Delta V^2{}_{DCin}$ and $\Delta V^2{}_{DCout}$ terms.

The displacement dependent force terms change the effective spring constant, similar to the effect of the output feedback force mentioned in the previous section. However, unlike the feedback force, the nonlinearity force works against the mechanical spring and softens it. Thus, the effective spring constant has to be updated as follows

$$k_{eff} = k_{mech} + k_{e,fb} - \Bigg[\underbrace{\frac{\varepsilon_0 A_{in}}{g_{in}^3}\left(\frac{V_{LO}^2}{2} + \Delta V_{DCin}{}^2\right)}_{k_{ein,nlin}} + \underbrace{\frac{\varepsilon_0 A_{out}}{g_{out}^3}\Delta V_{DCout}{}^2}_{k_{eout,nlin}}\Bigg]. \tag{2.44}$$

Now, it is also possible to compare the effects of the output feedback force and capacitor nonlinearity on the spring constant. Using (2.38) and (2.44), we can derive

$$\left|\frac{k_{e,fb}}{k_{eout,\,nlin}}\right| = \frac{C_{0out}}{C_{0out} + C_p}\,. \tag{2.45}$$

The design goals may favor an output capacitance as large as the load capacitance. Nevertheless, the relation $\left|k_{e,fb}/k_{eout,\,nlin}\right| \le 1$ is always valid. Thus, we conclude that spring never gets stiffer by reducing the gaps or increasing the voltages. We can now simplify (2.44) as follows

$$k_{eff} = k_{mech} - k_{ein,\,nlin} - k_{eout,\,nlin}\left(\frac{C_p}{C_{0out} + C_p}\right). \tag{2.46}$$

2.2 Mixer-Filter Design Specifications

A downconversion mixer has to satisfy certain performance requirements such as conversion gain, noise figure, and linearity, while an IF filter is mainly specified by its center frequency, bandwidth and insertion loss. As a MEMS mixer-filter combines mixing with filtering, it's performance is defined by the com-

bination of mixer and filter specifications. Thus, this section analyzes the mixer-filter center frequency, bandwidth, conversion-insertion gain, noise figure and linearity.

2.2.1 Center Frequency and Bandwidth

For the mixer-filter focused in this work, the center frequency is equal to the resonant frequency. Since the system has high Q, it is expected to be very close to the natural resonant frequency of the mass and spring. However, the non-idealities mentioned in the previous section shift the resonant frequency to $\omega_0 = \sqrt{\frac{k_{eff}}{m}}$, where k_{eff} is given by (2.46).

To analytically model the resonator's mechanical response, every element of the resonator is reduced to a component or force at the center of the electrode, and the cantilever beam itself is modeled as an Euler beam. Following this approach, both k_{mech} and m are calculated as point elements at the centroid of the square head, where the point force is presumably applied. Table 2-1 below is excerpted from Table 3-1 of [12] and summarizes the formulas for the calculation of the spring constant and the mass.

While the mechanical spring term is fixed for certain resonator dimensions, electrical spring terms vary with the applied voltages making the resonant frequency voltage-tunable. An ideal tuning mechanism would alter only the resonant frequency without affecting the other specifications. Because the gain is affected by either varying V_{LO} or ΔV_{DCout} (2.34), ΔV_{DCin} may be utilized solely for tuning purposes. The tuning range depends on the transducer dimensions and the permitted voltage range.

The Q also shifts due to the electrical spring and damper. Thus, the effective Q can be defined as

$$Q_{eff} = \frac{k_{eff}}{\omega_0 b_{eff}} = \frac{\sqrt{k_{eff} m}}{b_{eff}}. \tag{2.47}$$

Using this, -3 dB bandwidth can be simply given by

$$\Delta\omega_{-3dB} = \frac{\omega_0}{Q_{eff}} = \frac{\sqrt{\frac{k_{eff}}{m}}}{\frac{\sqrt{k_{eff} m}}{b_{eff}}} = \frac{b_{eff}}{m}. \tag{2.48}$$

. (2.49)

Table 2-2. Excerpt from Table 3-1 [12] with change in axis notation. Modeling equations for cantilever with a square head shown in Figure 2-1. Beam anchored at origin (0,0) extends along the y axis and the displacement is along the *x* axis. *I*: cantilever's moment of inertia, l_c: cantilever length, l_e: electrode length, w_c: cantilever width, w_e: electrode width, *h*: beam thickness, *E*: composite Young's modulus, ρ: composite density.

Cantilever beam shape	$x(y) = \frac{F}{EI}\left[-\frac{y^3}{6} + \left(\frac{l_e}{4} + \frac{l_c}{2}\right)y^2\right] \Leftrightarrow x(l_c) = \frac{F}{EI}\left(\frac{l_c^3}{3} + \frac{l_c^2 l_e}{4}\right)$
Reference deflection (at the center of electrode)	$x_{ref} = x\left(l_c + \frac{l_e}{2}\right) = x(l_c) + x'(l_c)\frac{l_e}{2} = \frac{F}{EI}\left(\frac{l_c^3}{3} + \frac{l_c^2 l_e}{2} + \frac{l_c l_e^2}{4}\right)$
Spring constant at the center of electrode	$k_{mech} = \frac{EI}{\frac{l_c^3}{3} + \frac{l_c^2 l_e}{2} + \frac{l_c l_e^2}{4}} = \frac{E w_c^3 h}{4l_c^3 + 6l_c^2 l_e + 3l_c l_e^2}$
Effective mass of cantilever beam	$m_{eff,\,beam} = \frac{m_{beam}}{l_c x_{ref}^2}\int_0^{l_c} x(y)^2 dy$
Effective mass of cantilever head	$m_{eff,\,head} = \frac{\rho l_e h}{x_{ref}^2}\int_{l_c}^{(l_c+w_e)} (x(l_c) + x'(l_c)(y-l_c))^2 dy + \frac{2\rho w_e h}{x_{ref}^2}\int_{(l_c+w_e)}^{(l_c+l_e-w_e)} (x(l_c) + x'(l_c)(y-l_c))^2 dy + \frac{\rho l_e h}{x_{ref}^2}\int_{(l_c+l_e-w_e)}^{(l_c+l_e)} (x(l_c) + x'(l_c)(y-l_c))^2 dy$
Effective mass of resonator	$m = m_{eff,\,beam} + m_{eff,\,head}$

2.2.2 Conversion-Insertion Gain

The conversion-insertion (c-i) gain of a mixer-filter is simply obtained by dividing the resonant output voltage amplitude by the input RF voltage amplitude. Using (2.34) and considering the electrical spring and damping, we get

$$G_{c-i} = \frac{|V_{out0}|}{|V_{RF}|} = \frac{\eta_{in}\eta_{out}}{b_{eff}\omega_0 C_p} = \frac{\varepsilon_0^2 A_{in} A_{out}\sqrt{m}}{2g_{in}^2 g_{out}^2 b_{eff}\sqrt{k_{eff}}(C_{0out}+C_p)} V_{LO}\Delta V_{DCout}. \quad (2.50)$$

The input and output transducers are usually designed to have equal feature sizes ($A_{in}=A_{out}=A$, $g_{in}=g_{out}=g$), due to the topological symmetry and the use of minimum gap obtainable from the CMOS-MEMS process in order to maximize both electromechanical coupling factors. In that case, the gain equation above can be re-written as follows

$$G_{c-i} = \frac{\varepsilon_0^2 A^2\sqrt{m}}{2g^4 b_{eff}\sqrt{k_{eff}}(C_{0out}+C_p)} V_{LO}\Delta V_{DCout}. \quad (2.51)$$

In a superheterodyne receiver, the active mixer usually provides conversion gain higher than the insertion loss of the IF filter making the total gain positive [1]. However, it is a challenge to get positive conversion-insertion gain from mixer-filters. In fact, substantial losses have been reported so far [6] [7]. To make mixer-filters practical, loss has to be reduced to acceptable levels, so that the sensitivity of the RF front-end is not dominated by the electrical noise of the subsequent preamplifier stage, as will be discussed in Section 2.2.3. Reduced loss also relaxes the gain required from the LNA and preamplifier, and thus reduces the overall power consumption.

Assuming that the effective damping is dominated by the mechanical damping (this assumption is valid unless extremely tiny gaps are used and will be numerically proven in Chapter 4), loss may be reduced by using larger electrode areas and narrower gaps. However, both feature sizes are currently limited by fabrication constraints. While the electrode height is determined by the thickness of the CMOS stack, the polymer buildup at the sidewalls sets the minimum gap spacing [7]. It is also not possible to use very large V_{LO} and ΔV_{DCout} as they are limited by on-chip and off-chip signal sources. It may be possible to reduce loss by

reducing the mechanical damping, which is dominated by anchor losses in vacuum [13]. However, it requires better understanding of the loss mechanisms in order to design better anchor structures. (2.51) also implies that the low-ω_0 mixer-filters have lower loss than their high-ω_0 counterparts. The MEMS channel-selectable architecture exploits this fact by employing low-ω_0 mixer-filters. Reducing the load capacitance is another way of improving gain. Therefore, the optimized preamplifier should provide minimum input capacitance. Also, the interconnects between the mixer-filter output and the preamplifier input should be kept as short as possible to keep parasitic capacitance minimum.

2.2.3 Noise Figure (NF)

Downconversion active mixers are usually noisy circuits which have to be preceded by low noise amplifiers (LNA) in order not to degrade the receiver sensitivity below an acceptable level [1]. Noise figure (*NF*) minimization plays a key role in the mixer design since the *NF* basically determines the preceding LNA's gain and thus power consumption. On the other hand, insertion loss of a passive filter is equal to its *NF* - for the impedance matched condition - and therefore has to be minimized. In this section, we will try to analyze the MEMS mixer-filter's noise behavior and formulate its *NF*.

Thermomechanical noise, the mechanical analog of Johnson noise, sets a limit for the sensitivity of the micromechanical mixer-filter. It is basically due to the coupling between the resonator and its environment (i.e. heat bath with many microscopic degrees of freedom). While this coupling causes the mechanical energy to leak away reducing resonator's Q, it also exposes resonator to constant random excitation by its interaction with the many microscopic degrees of freedom in the heat bath [17]. The result is that the lower the mechanical Q of the system, the larger the force noise. Hence, the minimum detectable force is determined by the force noise that is given by

$$\sqrt{\frac{\overline{F_n^2}}{\Delta f}} = \sqrt{\frac{4k_B T k_{eff}}{Q_{eff}\omega_0}} = \sqrt{4k_B T b_{eff}}. \qquad (2.52)$$

Referring the force noise to the input gives the minimum detectable RF amplitude as

$$\sqrt{\frac{\overline{V_{n,\,tmech}^2}}{\Delta f}} = \frac{\sqrt{4k_BTb_{eff}}}{|\eta_{in}|} = \frac{2g_{in}^2\sqrt{4k_BTb_{eff}}}{\varepsilon_0 A_{in}V_{LO}}. \tag{2.53}$$

Given the source noise is $\overline{V_{n,\,s}^2} = 4k_BTR_{sRF}\Delta f$, the mixer-filter *NF* can be simply derived by dividing the total input-referred noise power by the source noise power.

$$NF = \frac{\overline{V_{n,\,s}^2} + \overline{V_{n,\,tmech}^2}}{\overline{V_{n,\,s}^2}} = 1 + \frac{\overline{V_{n,\,tmech}^2}}{\overline{V_{n,\,s}^2}} = 1 + \frac{4g_{in}^4 b_{eff}}{\varepsilon_0^2 A_{in}^2 V_{LO}^2 R_{sRF}}. \tag{2.54}$$

We can conclude from the equation above that the *NF* minimization requires narrow gaps, large electrode areas, small damping and large LO amplitudes (we are again assuming that the damping is dominated by the mechanical damping as will be discussed in Chapter 4). It can now be said that the *NF* minimization faces similar challenges with the loss minimization mentioned in the previous section. In an integrated system, it is also possible to design the preceding LNA to provide a source resistance larger than 50 Ω in order to improve the *NF* of the mixer-filter.

To better point out the mixer-filter's contribution to the total front-end noise, we have to go one step further and refer the electrical noise from the preamplifier to the input of the mixer-filter. Then, we find the system *NF*, NF_{sys}, by dividing the total input-referred noise power by the source noise power, and it is given by

$$NF_{sys} = \frac{\overline{V_{n,\,s}^2} + \overline{V_{n,\,tmech}^2} + \overline{V_{n,\,elec}^2}}{\overline{V_{n,\,s}^2}} = 1 + \frac{1}{R_{sRF}}\left(\frac{4g_{in}^4 b_{eff}}{\varepsilon_0^2 A_{in}^2 V_{LO}^2} + \frac{\overline{V_{n,\,preamp}^2}}{4k_BTG_{c-i}^2}\right) \tag{2.55}$$

where $V_{n,elec}$ is the input-referred electrical noise and $V_{n,preamp}$ is the electrical noise at the preamplifier input.

2.2.4 Linearity

The upper limit of the dynamic range of a communication device is set by nonlinear distortion. Fundamentally, the more linear a device, the better it can deal with large input signals and interferers. Thus, this section analyzes the linearity of the MEMS mixer-filter.

The MEMS mixer-filter shown in Figure 2-5 has the following inherent nonlinearities: (i) The ΔV^2_{in} term in the force equation quadratically mixes the signals (ii) As the displacement-to-gap ratio increases, higher-order terms from $\partial C / \partial x$ start to contribute to the intermodulation (IM) products (ii) For large enough displacements, the mechanical nonlinearities of the MEMS structures also become important [14].

As already shown in Section 2.1.1, the mixing behavior is based on (i) above. However, this desired nonlinearity may also cause undesired IM2 products. As shown in Figure 2-6, the interferers spaced ω_0 apart either from the signal or between themselves would generate forces overlapping with the desired mixer force. The mixer and IM2 force terms can be related to voltage inputs as follows

$$\begin{aligned} F_{mixer} &\propto (V_{RFsig} V_{LO}) \\ F_{IM2} &\propto (V_{RFsig} V_{RFintA} + V_{RFintB} V_{RFintC}) \end{aligned} . \tag{2.56}$$

Although LO amplitude is relatively high, the interferers, which have already been amplified by the preceding LNA, may be sufficiently large to obscure the desired signal. Worse, there may exist multiple ω_0 spaced interferer couples, each adding to the IM2 force. Nevertheless, it is possible to suppress IM2 distortion using certain design techniques [21]. These include filtering the interferer signals before the mixer-filter and employing a differential topology. Filtering the interferers would require filters with GHz center frequencies and MHz bandwidths, and the design of such a filter would be more challenging than the design of the mixer-filter itself. Thus, it is more practical to reject the IM2 distortion using the differential topology shown in Figure 2-7. It employs two identical mixer-filters that are driven by the same RF and differential LO signals. Mixing with differential LO causes the output signal to be differential while the IM2 products

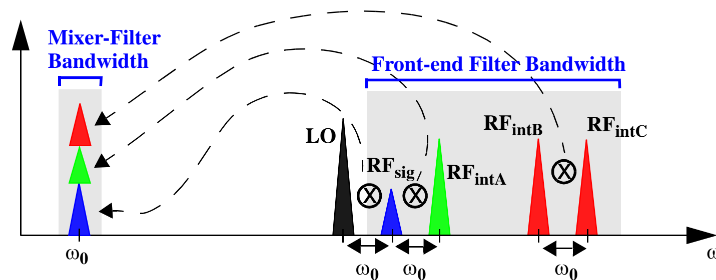

Figure 2-6 Second-order intermodulation (IM2) products due to the quadratic force relation.

occur in phase. The subtraction at the output cancels the IM2 terms while giving out a doubled signal term. Since it is practically impossible to obtain perfect matching between the differential mixer-filters, such a design would require separate DC potentials across the input and output transducers for the gain and frequency tuning. Besides, the mismatch problem can be eliminated by differentially driving a single cantilever as demonstrated in [11].

In a perfectly matched differential topology, all the IM forces generated by the interaction of the interferers within themselves and with the desired signal occur in-phase, and are therefore cancelled. Since the LO is the only signal that can shift the force phases, we only need to be concerned about the interaction of the LO signal with the interferers. Derivation of the IM products generated by such interactions is quite involved and falls beyond the scope of this work. However, we may benefit from the IIP3 formulation presented in [16] to get an idea about the 3rd order nonlinearity of the mixer-filters. [16] analyzes IM3 distortion for the micromechanical filters in the presence of two input tones and considers only the lower-sideband IM3 terms. Correspondingly, for the mixer-filter, we will consider the LO as the first tone, and the second tone will be located at $2\omega_{LO}$-ω_0 so that the lower-sideband IM3 product falls into the mixer-filter passband. Using (11) from [16], the tone amplitude at the IIP3 can be expressed as

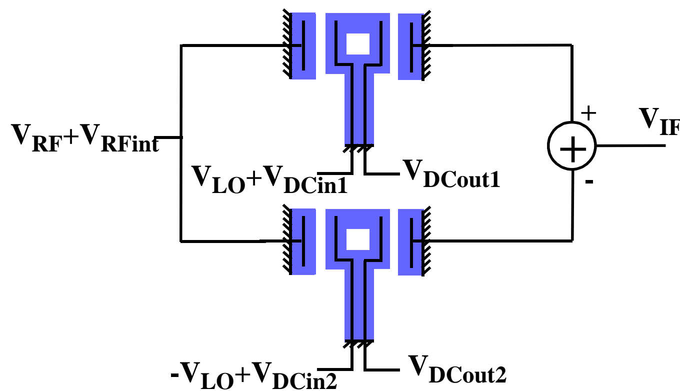

Figure 2-7 An example of IM2-reject mixer-filter.

$$V_{IIP3} = \left[\frac{\varepsilon_0 A_{in}}{4g_{in}^3 k_{eff}}(2\Theta_{LO} + \Theta_{int}^*) + \frac{3\varepsilon_0^2 A_{in}^2 \Delta V_{DCin}^2}{4g_{in}^6 k_{eff}^2}\Theta_{LO}(\Theta_{LO} + 2\Theta_{int}^*) + \frac{3\varepsilon_0^3 A_{in}^3 \Delta V_{DCin}^4}{2g_{in}^9 k_{eff}^3}\Theta_{LO}^2\Theta_{int}^*\right]^{-1/2} \quad (2.57)$$

where $\Theta_{LO} = \Theta(j\omega_{LO})$ and $\Theta_{int} = \Theta[j(2\omega_{LO} - \omega_0)]$, and can be obtained using (2.13).

The two tones at a filter input may be located close to its center frequency while the mixer-filter inputs are typically very far from its passband. Thus, the mixer-filters are expected to be more immune to IM3 distortion than their filter counterparts. Besides, the mixer-filter displacement is typically much smaller than the resonator length, so that we can leave mechanical nonlinearities out of consideration.

2.3 Image Rejection

In a superheterodyne architecture, the bands symmetrically located above and below the LO frequency are downconverted to the same IF. Therefore, a possible interferer located at the image frequency of the desired signal have to be suppressed around 60-70 dB for adequate communication in most RF applications [1]. Even though an RF bandselect filter provides some attenuation at the image frequency when LO signal is out-of-band (as shown in Figure 2-6), its rejection might not be sufficient to suppress the possibly much higher signal emissions in the adjacent bands. Besides, if the system is required to use an in-band LO, a large in-band image may totally obscure the desired signal. Therefore, an image-reject architecture is inevitable. Hartley image-reject architecture [1] is a possible solution. Figure 2-8 illustrates an example topology in which the Hartley image rejection follows the IM2 rejection proposed in Section 2.2.4.

In this chapter, we have developed an analytical understanding of the mixer-filter operation and design considerations. Chapter 3 focuses on the mixer-filter modeling and simulations while Chapter 4 demonstrates and compares the analytical, simulated and measured results.

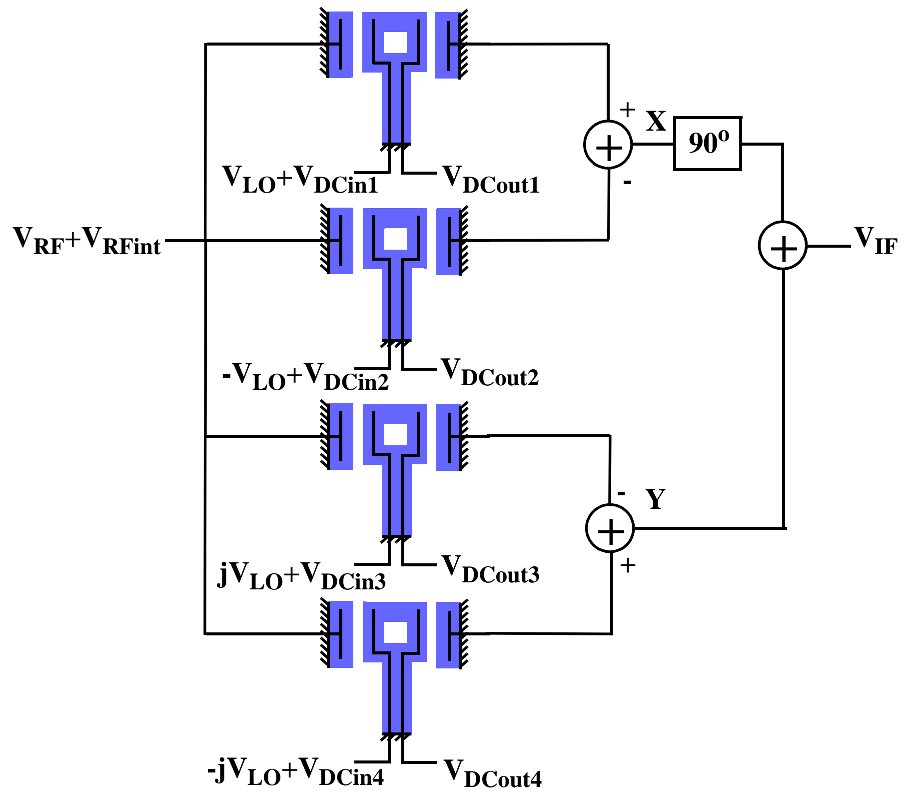

Figure 2-8 An example of IM2 + image reject mixer-filter.

3 Computer Aided Design of CMOS-MEMS Mixer-Filters

We have shown in Chapter 2 that the MEMS mixer-filter design optimization, very similar to electrical circuit design optimization, involves nontrivial trade-off analyses that necessitate the use of CAD tools. Therefore, we need an accurate resonator model and a simulation environment that offers MEMS-integrated circuit (IC) co-simulation together with fast and accurate RF analyses. NODAS, a set of lumped element electromechanical models developed at Carnegie Mellon University [9], gives us the capability to build a mixer-filter model from the atomic elements. NODAS uses the Verilog-A hardware modeling language and can be simulated using Cadence Spectre and SpectreRF simulators. Due to its compatibility with the IC design tools, NODAS also enables parasitic layout extraction, which is crucial in high-frequency design. In summary, NODAS:

- Enables MEMS-IC co-design,
- Offers the capability to model and simulate various resonator topologies,
- Enables trade-off analyses for design optimization,
- Allows parasitic layout extraction and verification offered by state-of-the-art IC design tools (e.g. Cadence Calibre),
- Speeds up the design process for a large array of mixer-filters,
- Allows design automation using tools such as Cadence Virtuoso NeoCircuit.

3.1 NODAS Cantilever Resonator Model

The NODAS library contains three atomic elements: beams, plates and electrostatic gaps. A MEMS mixer-filter, which is essentially composed of micromechanical resonators and electromechanical transducers, can be modeled using these elements.

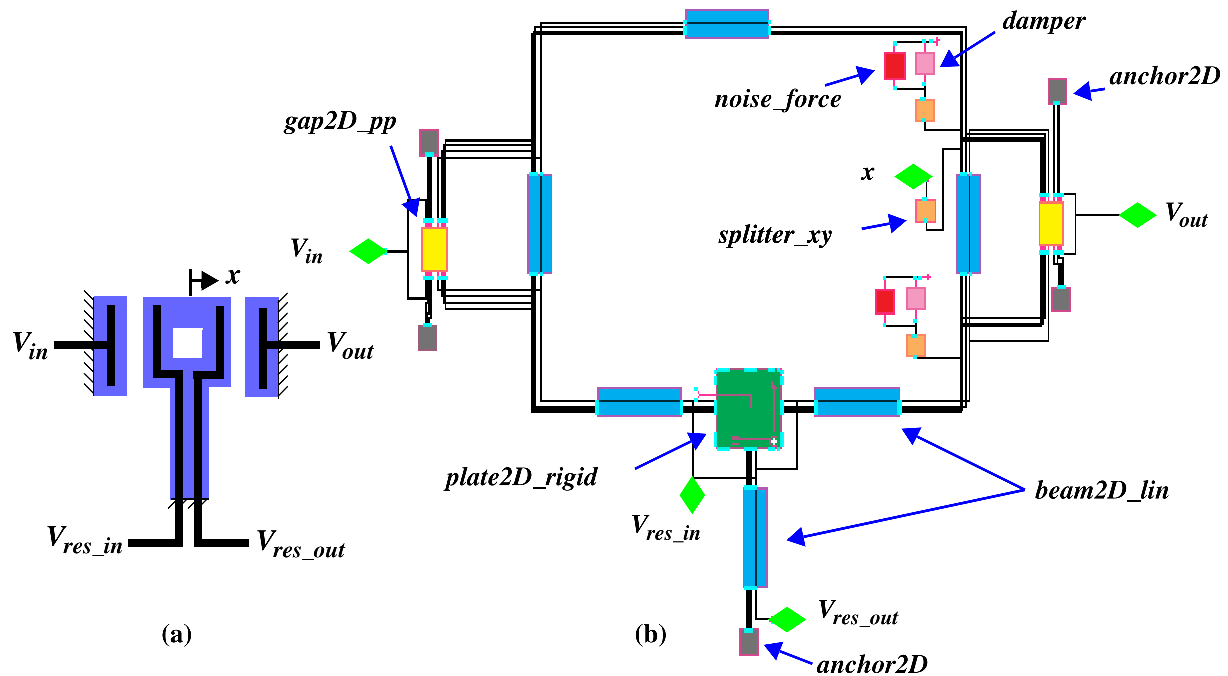

Figure 3-1 The cantilever mixer-filter: **(a)** Illustration **(b)** NODAS model.

Figure 3-1. shows both the illustration and the NODAS model of the cantilever mixer-filter that is focused in this work. Because the plane of motion is 2D (*x-y* plane) and the displacement is usually limited by narrow electrostatic gaps, the 2D linear beam element (cell name: *beam2D_lin*) is utilized as the main building block for the mechanical structure. A 2D rigid plate (cell name: *plate2D_rigid*) is used to accurately model the triple joint between the cantilever beam and the two head beams. The 2D gap elements (cell name: *gap2D_pp*) in the model are the key components for electromechanical operation as they take care of the force and current generation at the transducers. Another NODAS element, the 2D anchor (cell name: *anchor2D*) is used to fix the one end of the cantilever and the stator electrodes. The *splitter_xy* cell in the model is used to obtain the *x* position from a node carrying (*x*,*y*) position information. Since NODAS currently doesn't model anchor losses, which damp the resonator in vacuum, we have added simple *damper* elements to the model. We have also included *noise_force* elements in order to model the thermomechanical noise.

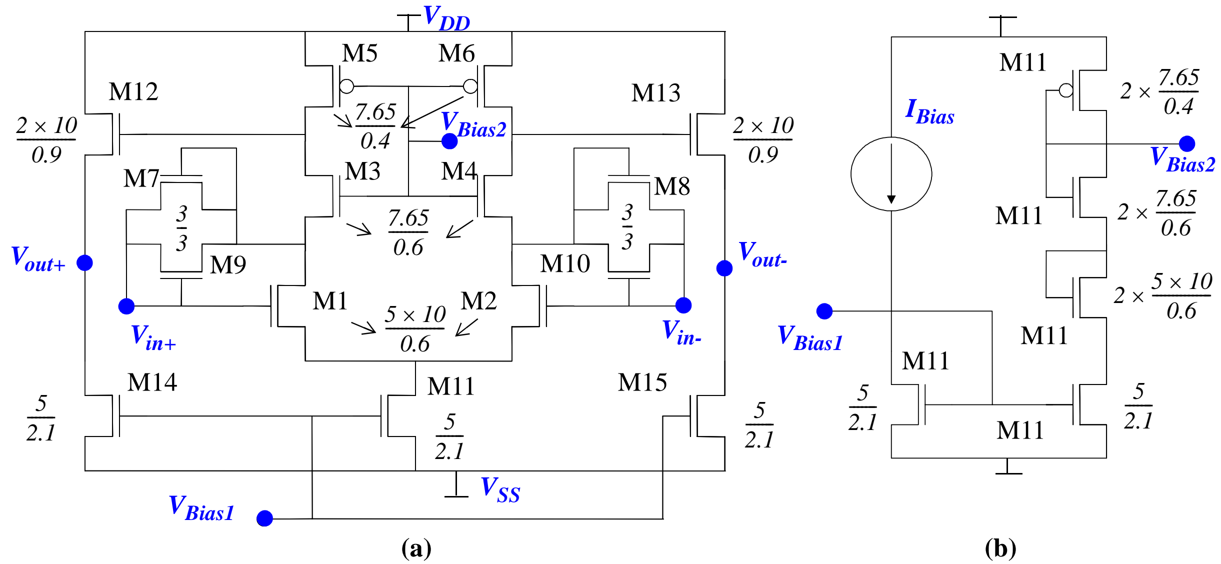

Figure 3-2 Preamplifier schematic with W/L ratios **(a)** Differential amplifier with source follower output stages **(b)** Biasing stage.

The model parameters include mechanical dimensions - beam lengths and widths, transducer gap spacing -, material properties - composite Young's modulus (E) and composite density (ρ), (See Table 2-2 in Chapter 2)- and environment properties - temperature. The mechanical damping coefficient (b_{mech}) is also a parameter which has to be obtained from the measured Q using the relations (2.39) and (2.47) given in Chapter 2. The model includes pins for the input/output voltages - V_{in}, V_{res_in}, V_{res_out}, V_{out}. In addition, the displacement in the x axis - x - is brought out as an I/O pin to obtain deeper information from the simulation.

3.2 Preamplifier

The preamplifier used in this work was originally designed as a capacitive sense circuit for CMOS-MEMS accelerometers [19]. Although not optimized for use with CMOS-MEMS mixer-filters, it was considered appropriate as a preliminary design due to its good input impedance, noise and gain performance.

Figure 3-2 shows the preamplifier schematic, which comprises a differential amplifier with the source follower output stages and a biasing stage. The input nodes of the preamplifier are biased by the tran-

sistor pairs M7-M9 and M8-M10 working in the subthreshold region. Without those, leakage current paths would charge the input gate capacitance to the power supply rails [19]. Since the input capacitance value has to be kept minimum to better sense the motional current from a MEMS device, the cascode transistors M3-M4 are used to reduce the Miller effect between the input and output nodes. The source follower stages drive the large bondpad capacitors. The bias current, I_{Bias}, is provided by an on-board resistor connected between the nodes V_{DD} and the M11 drain.

The preamplifier circuit was designed and implemented in Jazz Sige60 process. The simulated preamplifier performance is given in Table 3-1.

Table 3-1. Simulated preamplifier performance for V_{DD} = 5 V, V_{SS} = Gnd = 0 V and I_{Bias} = 200 μA.

DC Gain (*A*)	38 dB
-3 dB Bandwidth	61.0 MHz
Input capacitance (C_p)	150 fF
Input referred noise current @ 1 MHz	5.5 fA/sqrt(Hz)
Power consumption	5 mW

3.3 Differential Mixer-Filter Topology

As illustrated in Figure 3-3, each CMOS-MEMS mixer-filter cell is designed as a differential system consisting of differential resonators and a differential preamplifier. Such a topology provides a significant advantage that any parasitically coupled high-frequency signal (RF or LO) appears as a common-mode signal at the preamplifier's input and therefore rejected. We did not use differential LOs in this work. However, the cell can be easily modified to have two separate LO inputs in order to build the IM2 + image reject architecture shown in Figure 2-8 of Chapter 2.

3.4 Mixer-Filter Array Layout

This work utilized the bottom three metal layers (M1, M2 and M3) of the CMOS process as the structural layers for the cantilever mixer-filter. The metal layers were also used as the interconnects that

carry the electrical signals to the transducer electrodes. Besides, they were stepped at the sidewalls to alleviate the undesired effects of CMOS mask misalignment [13].

The designed and fabricated array comprises a set of differential mixer-filters each resized to have a unique combination of a certain resonant frequency and gap spacing. The design utilizes 8 different resonant frequencies (from ~500 kHz to ~1.2 MHz in ~100 kHz steps) and 2 different gap spacing (0.5 and 0.8 μm) constituting a total of 16 combinations.

The layout design has targeted minimum parasitic coupling between the high-frequency and the low-frequency signals in order to avoid any spurious product that might occur due to the inherent nonlinearities in the system. As shown in Figure 3-4a the high-frequency pads have been placed far away from the low-frequency pads to minimize the coupling between the bondwires that connect the die pads to the board pins. Also, the high-frequency interconnects have been well isolated from the low-frequency ones, either by avoiding wire-crossovers or putting grounded shields in between (Figure 3-4b).

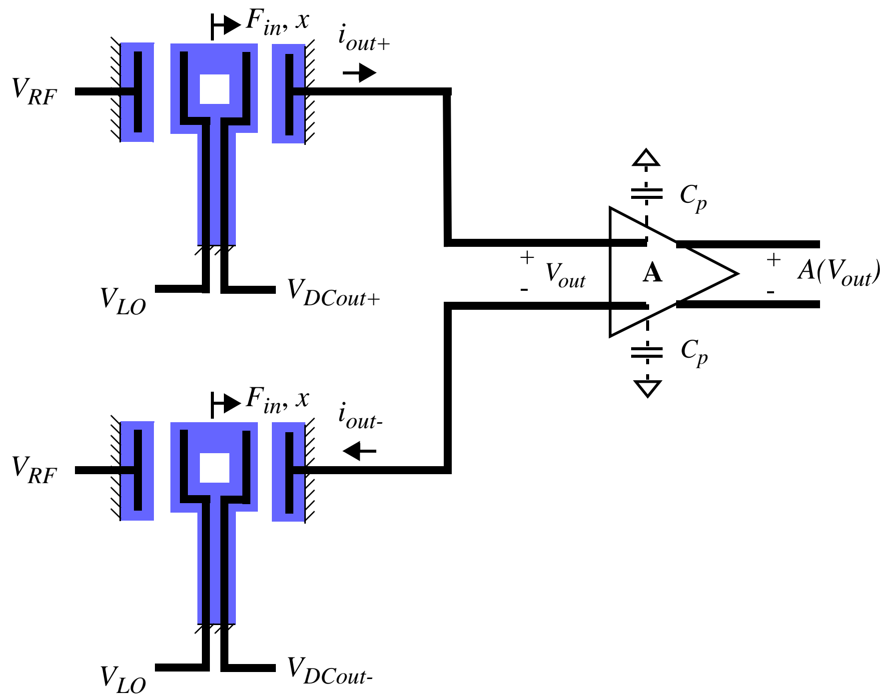

Figure 3-3 Differential Mixer-Filter.

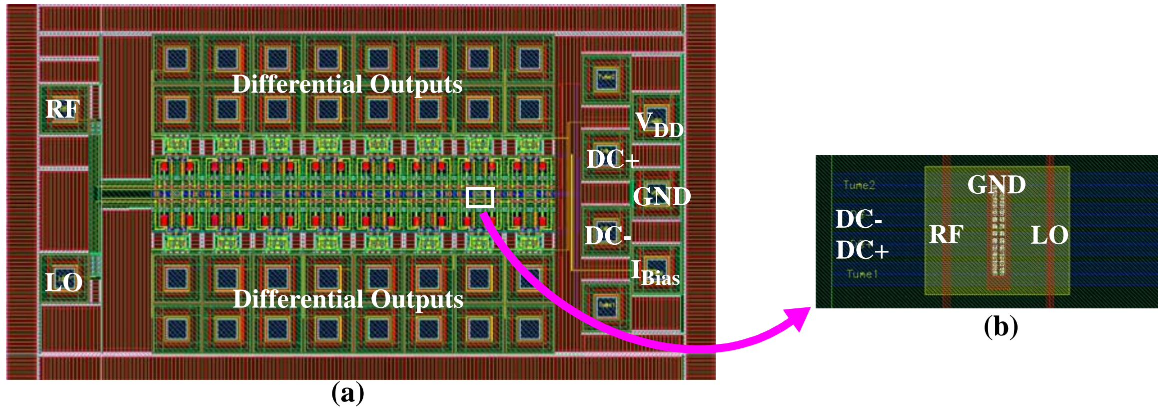

Figure 3-4 **(a)** Complete layout **(b)** Grounded shield between RF/LO and DC+/DC-.

3.5 Simulations

Conventional analyses provided by Spice-like simulators are mostly inefficient in simulating frequency conversion systems such as front-end mixers. An AC analysis simulates a system at a single frequency and therefore incapable of frequency conversion. A transient analysis, on the other hand, can simulate frequency conversion, however the simulations take a very long time when there is a large separation between the highest and the lowest frequency in the system. Moreover, the mixer-filter requires one of the input frequencies (RF or LO) to sweep in order to observe the filtering function. Although this is theoretically possible using a sequence of transient analyses, the high mechanical *Q* of the mixer-filter requires tiny frequency steps each having a very long stabilization time, which make the simulations practically useless for an iterative design. Therefore, in this work, we benefit from Cadence SpectreRF [20] simulator, which provides periodic large-signal and small-signal analyses for the simulation of frequency conversion effects.

The large-signal analysis (PSS) computes the periodic steady-state response of a circuit at a specified fundamental frequency, with a simulation time independent of the time-constants of the circuit. The PSS basically linearizes the circuit about a time-varying large-signal operating point. It is followed by a periodic small-signal analyses (PXF or Pnoise) that use the time-varying operating point to compute the circuit response to a small sinusoid at an arbitrary frequency. Any number of small-signal analyses can be per-

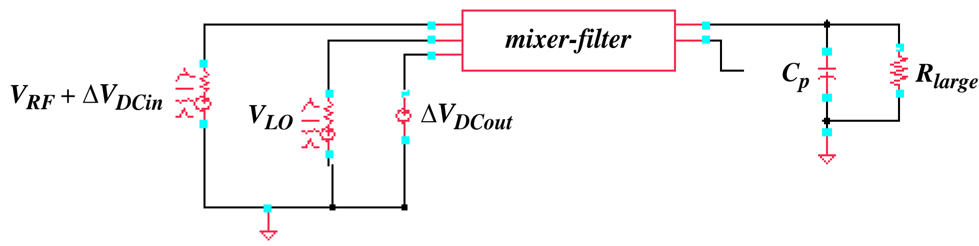

Figure 3-5 Mixer-filter testbench.

formed following a large-signal analysis. This two-step process is capable of simulating frequency conversion effects. For the mixer-filter simulation, the large-signal stimulus is the LO signal while the RF is applied as the small-signal.

Besides a fast and accurate simulator, we also need testbenches for simulating the mixer-filter performance. In this work, we have used three testbenches: Mixer-filter testbench, schematic and extracted system testbenches.

3.5.1 Mixer-filter Testbench

Figure 3-5 shows the Cadence testbench used for the mixer-filter simulations. The voltage inputs are provided using ports, which have finite impedances, and sources. The mixer-filter output is terminated with a load capacitor (C_p) and biased using a very large resistor (R_{large}). Using this testbench, we simulate the performance of a single mixer-filter for varying design parameters such as the mechanical dimensions, source and load impedances, and the input voltages. We also use the simulated data to verify the analytical model built in Chapter 2.

3.5.2 System Testbench

We also need a testbench that is consistent with the physical testbench, so that we can simulate the whole system (differential mixer-filters + preamplifier + buffer) and compare the results with the measured data. Such a testbench would also allow us to observe the total system performance and make system trade-offs.

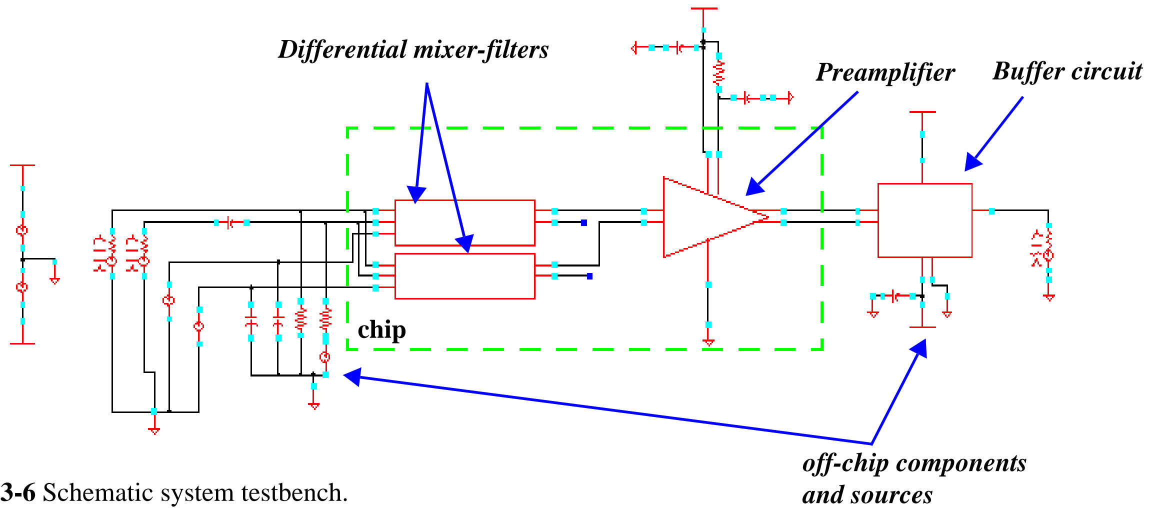

Figure 3-6 Schematic system testbench.

Figure 3-6 shows the Cadence schematic testbench used for the system simulations. The green dotted rectangle symbolizes the chip boundary, which encloses the differential mixer-filters and the preamplifier. The testbench also includes off-chip sources, components and circuits.

The designed layout requires verification through parasitic extraction and simulation. Since IC extraction tools do not extract MEMS devices, we have to replace the MEMS mixer-filter with its NODAS schematic model and then extract the rest of the layout that includes the interconnects and the electrical circuits. Thus, we can simulate the parasitics effects and preserve the MEMS functionality at the same time.

Figure 3-7 shows the extracted testbench in which the chip boundary encloses the differential mixer-filters and the extracted layout. For parasitic extraction, we use the Calibre tool provided by the Jazz design kit.

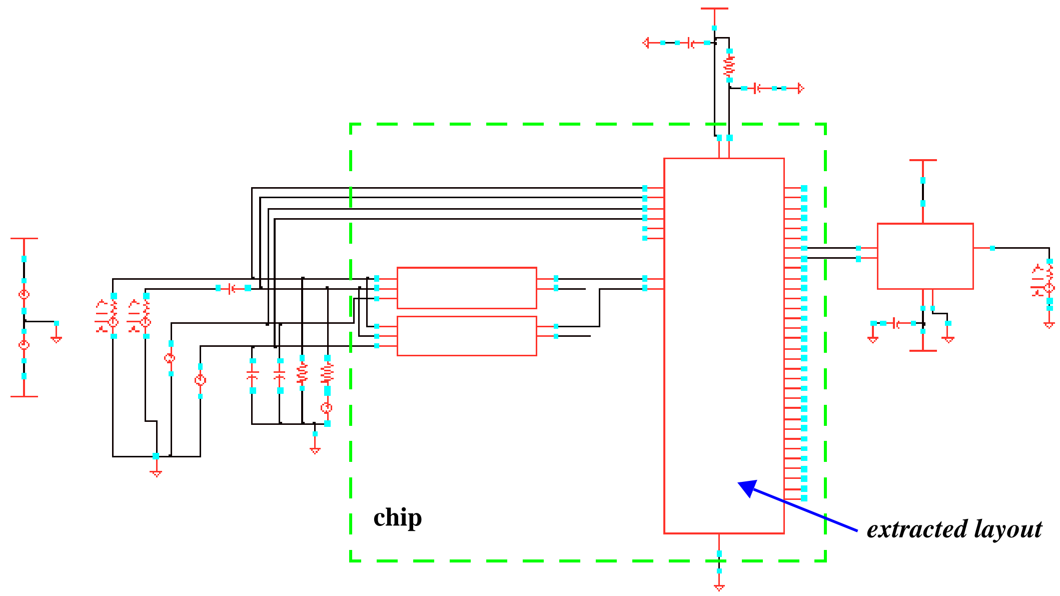

Figure 3-7 Extracted system testbench.

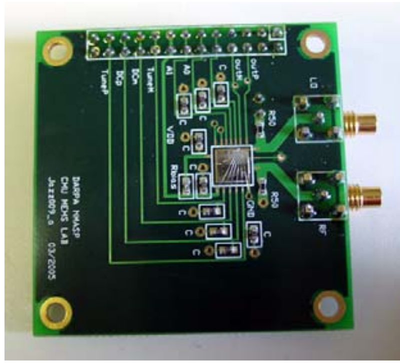

(a)

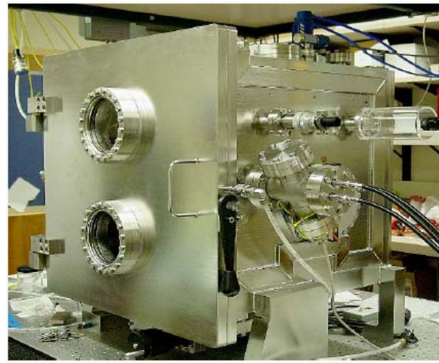

(b)

Figure 4-1 **(a)** PCB with chip wirebonded **(b)** Vacuum chamber capable of sub-1m Torr.

4 Results

The MEMS mixer-filter has to operate in vacuum in order to minimize air damping and maximize mechanical *Q*. Thus, the post-processed chip is wirebonded onto a custom printed-circuit-board (PCB) and placed in a vacuum chamber for testing (Figure 4-1).

4.1 PCB Design and Characterization

The PCB has been designed using Circuitmaker/Traxmaker software tools. It is 2” by 2” in size with four SMC connectors for high-frequency inputs and the differential outputs, and a 26 pin connector for DC signals. To save space, surface-mount-devices (SMD) have been used as on-board resistors and capacitors.

Because a MEMS mixer-filter converts the input voltage, not the input power, into electrostatic force, a good design requires maximum voltage transfer at its input rather than maximum power transfer. However, the maximum voltage transfer necessitates impedance mismatches and thus signal reflections which would prevent us from knowing the exact the voltage at the mixer-filter input. Then, it would be

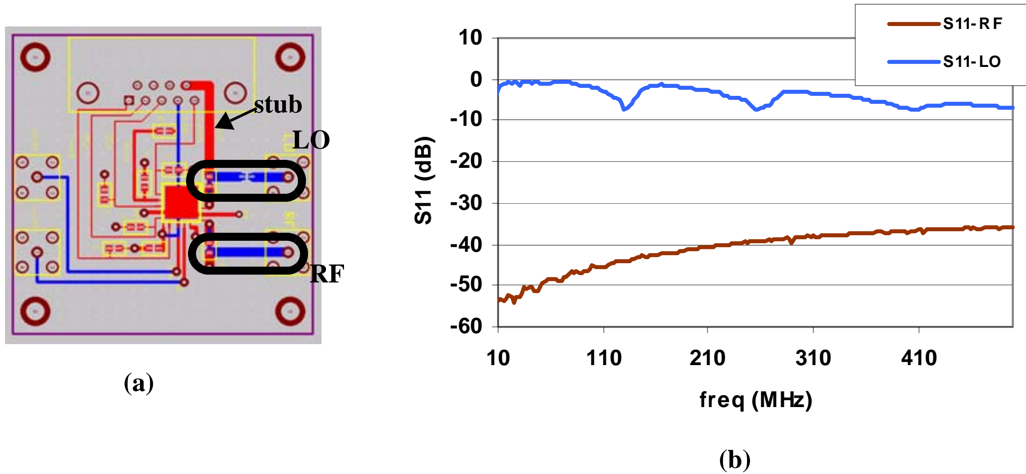

Figure 4-2 (a) PCB Traxmaker schematic with highlighted RF and LO traces **(b)** Measured S11 for RF and LO ports.

impossible to characterize the conversion-insertion gain. Therefore, we exploit impedance matching to prevent reflections and make sure that the voltage amplitude read from the signal generator equals to the voltage amplitude at the mixer-filter input. To achieve impedance matching, RF and LO traces have been designed as 50 ohm microstrip lines and terminated with 50 Ω on-board resistors.

The S11 parameters measured for the connector + microstrip line + resistor combination sweeping a frequency range from 10 MHz to 500 MHz (network analyzer limit) are plotted in Figure 4-2b. It demonstrates that the RF port is very well matched giving an S11 below -30 dB across the frequency range. However, the LO port is not well matched with S11 above -10 dB. It is most probably because the stub that is used to carry the DC offset signal, which is ground in this measurement, act as a transmission line and convert the short-circuit impedance to a higher impedance that is in series with the 50 Ω termination resistor. This is a design error that can be either corrected by eliminating the LO DC offset or adding it via a very large resistor connected in parallel with the 50 Ω resistor.

4.2 Measured Results

We make a two-step measurement to characterize the CMOS-MEMS mixer-filters. First, we direct-drive them to determine resonators' fundamental characteristics such as the resonant frequency and the Q.

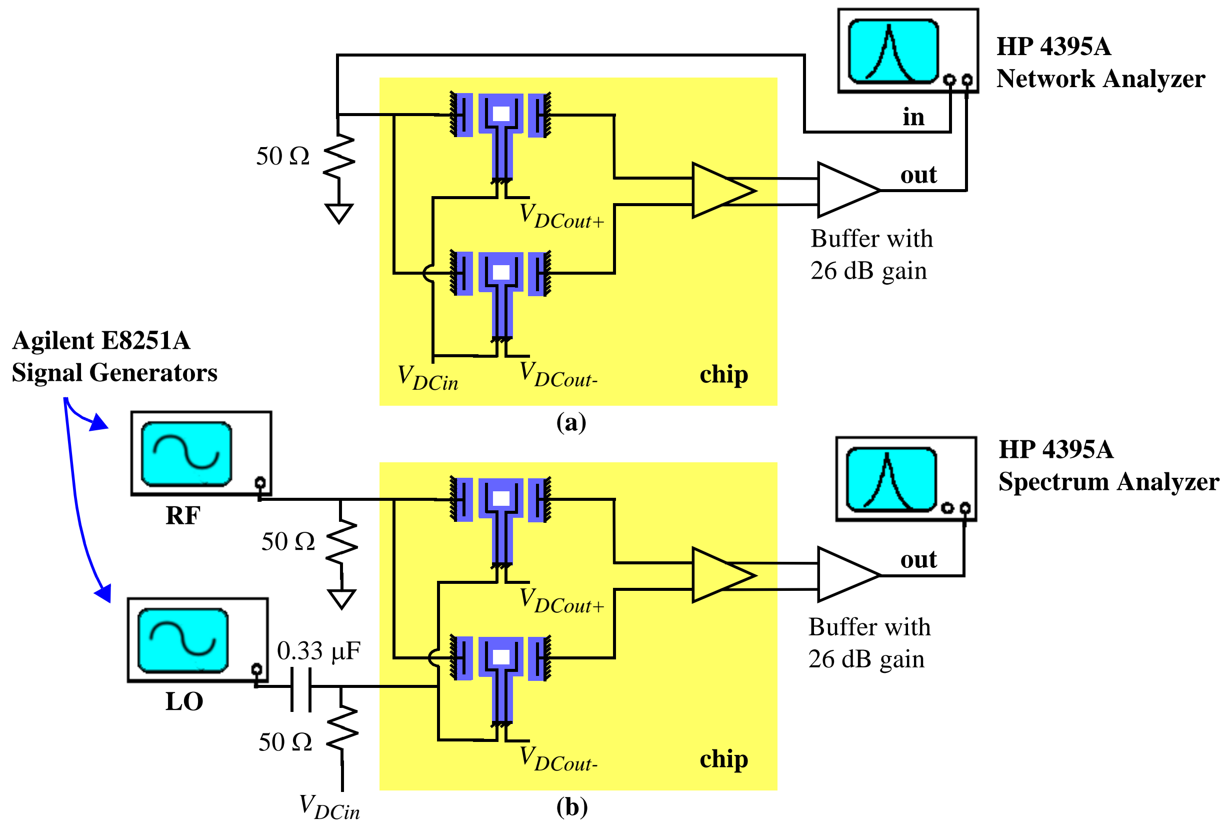

Figure 4-3 (a) Direct-drive test setup **(b)** Mixing test setup.

Figure 4-3a illustrates the test setup for the direct-drive measurement in which a network analyzer (NA) is used to measure the filter's insertion loss. A DC potential, V_{DCin}, is applied to the resonator's input electrode to generate an electrostatic force at the input frequency and the mechanical displacement is detected with the use of differential DC potentials, V_{DCout+} and V_{DCout-}. For mixing measurements, we use two high-frequency signal generators as the RF and LO sources, and the IF output is connected to a spectrum analyzer (SA). V_{DCin} is added to the LO signal via a 50 Ω resistor and decoupled from the LO source with a large on-board capacitor. In both setups, an offchip amplifier is used as a buffer in order to drive the 50 Ω input impedance of the NA/SA. It also converts preamplifier's differential output into a single-ended output.

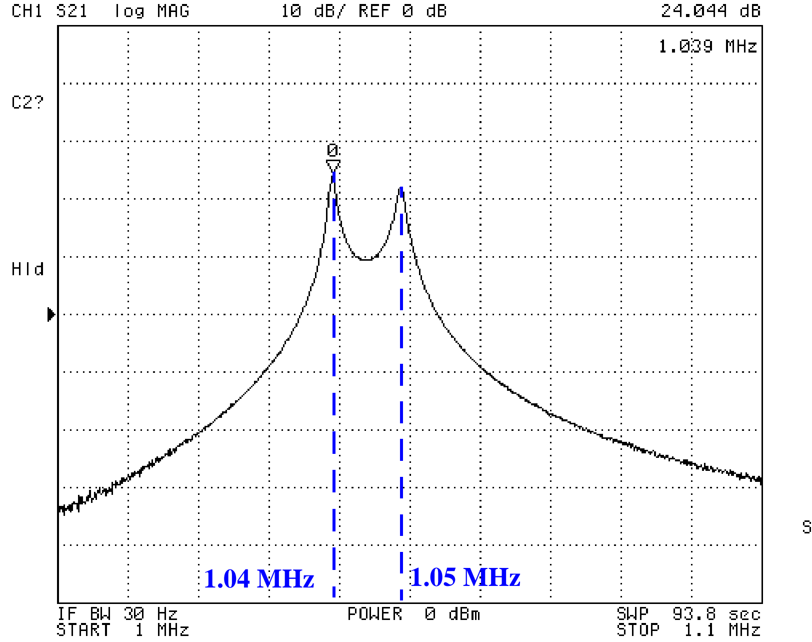

Figure 4-4 Resonator frequency characteristics under 100 mTorr pressure with $V_{DCin} = V_{DCout+} = V_{DCout-} = 10V$.

This work presents the test results only for one of the mixer-filters in the array. Both the drawn and the measured dimensions of the tested mixer-filter is listed in Table 4-1.

Table 4-1. The dimensions of the tested mixer-filter. l_c: cantilever length, l_e: electrode length, w_c: cantilever width, w_e: electrode width, g: transducer gaps.

	Drawn (μm)	*Measured (μm)*
l_c	21.5	20.1
w_c	1	1.5
l_e	7	7.5
w_e	1	1.6
g	0.8	0.8

4.2.1 Resonator Characteristics

We first determine the frequency mismatch between the differential resonators by applying the same voltage across their output transducers. As plotted in Figure 4-4, the system output has two peaks at frequencies 1.04 and 1.05 MHz, which implies a frequency mismatch of 10 kHz (%1). Since the RF and LO inputs are shared between the differential resonators, electrostatic tuning might be only possible by changing the output DC potentials as done in [7]. However, the tuning range, which is practically limited by the

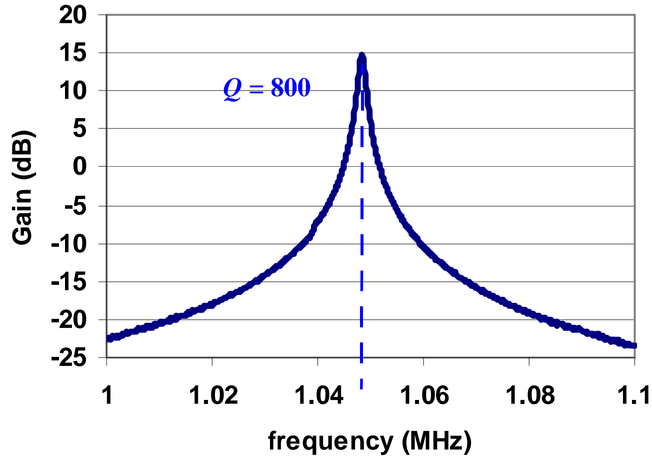

Figure 4-5 Measured system response under 100 mTorr vacuum with $V_{DCin} = V_{DCout+} = 10$V, and $V_{DCout-} = V_{bias} = 1.65$ V.

maximum voltage provided by the power supply, has been smaller than 10 kHz. Therefore, we have chosen to kill one of the peaks by making either V_{DCout+} or V_{DCout-} equal to the preamplifier's input bias voltage, which is notated as V_{bias}. Doing that gives the system response plotted in Figure 4-5. The cantilever resonates at 1.05 MHz with a Q of 800 under 100 mTorr vacuum. The measured system gain is 15 dB.

4.2.2 Mixer-Filter Characteristics

For mixing measurements, we switch to the test setup illustrated in Figure 4-3b. Figure 4-6a plots the measured gain vs. IF frequency for three different LO frequencies (100, 200 and 300 MHz) and the RF frequency swept from f_{LO}+1 to f_{LO}+1.1 MHz. The system response has a peak at 1.05 MHz with a total gain of -8 dB, which distributed between the system blocks as shown in Figure 4-6b. Subtracting the gain provided by the amplifiers gives a mixer-filter conversion-insertion loss of 72 dB.

For this work, we have only characterized the resonant frequency, Q (thus bandwidth) and the conversion-insertion loss of a cantilever mixer-filter. Table 4-2 below summarizes the measured data and com-

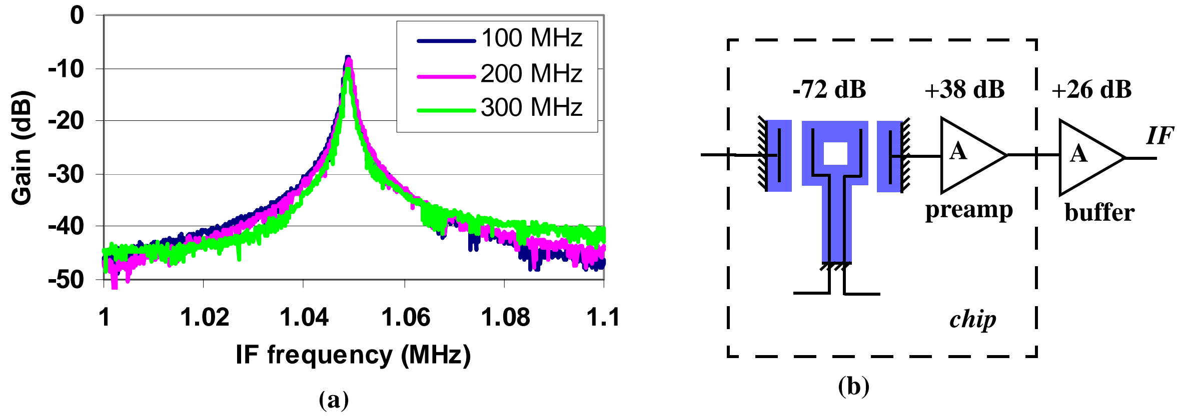

Figure 4-6 (a) Measured system gain for f_{LO} stepped from 100 to 300 MHz with V_{LO} = 1.4 V, V_{DCout+} = 10 V, V_{DCout-} = V_{bias} = 1.65 V. **(b)** Gain distribution between the system blocks.

pares with the analytical values obtained from the model built in Chapter 2 and the data from the NODAS simulations described in Chapter 3. It also lists the analytical and simulated values for the *NF* and V_{IIP3}.

Table 4-2. Comparison of analytical, simulated and measured data for center frequency (f_0), -3 dB bandwidth (Δf_{-3dB}), conversion-insertion gain (G_{c-i}), mixer-filter + preamplifier gain (G_{sys}), mixer-filter noise figure for 50 Ω source resistance (*NF*), mixer-filter + preamplifier noise figure for 50 Ω source resistance (NF_{sys}), input third intercept point (V_{IIP3}).

	Analytical	**Simulated**	**Measured**
f_0	1.03 MHz	1.18 MHz	1.05 MHz
Δf_{-3dB}	1.3 kHz	1.5 kHz	1.3 kHz
G_{c-i}	-68 dB	-72 dB	-72 dB
G_{sys}	-	-34 dB	-34 dB
NF	88 dB	85 dB	-
NF_{sys}	-	102 dB	-
V_{IIP3}	88 dBV	-	-

As seen from the table above, there is an 18% mismatch between the simulated and measured resonant frequency and bandwidth. However, this is acceptable considering the uncertainties in the measured resonator dimensions and the material properties. We have also obtained a good agreement between the simulated and measured gain. Besides, the calculated values are quite close to the simulated and measured data indicating the accuracy of the analytical model built in Chapter 2. On the other hand, the expected *NF* and V_{IIP3} are excessively higher than the typical mixer values, which makes their measurements impractical.

4.3 Specifications vs. Design Parameters

As can be concluded from the data listed in Table 4-2, the presented work is far from achieving an acceptable performance in terms of conversion-insertion loss and the noise figure. Thus, the design has to be improved by resizing the design parameters. In this section, we will demonstrate how the specs change with varying certain design parameters. We will present both the analytical and the simulated data, and this will also serve the purpose of verifying the analytical model proposed in Chapter 2. We have obtained the simulated data using the mixer-filter testbench described in Section 3.5.1 of Chapter 3.

4.3.1 Resonant (Center) Frequency

Figure 4-7 below plots the resonant frequency vs. gap (input and output gaps are equally sized), LO voltage amplitude, DC potential across the output transducer, and the load capacitance. It demonstrates that the analytical trends are in good agreement with the simulated trends with a ~10% mismatch in the resonant frequency.

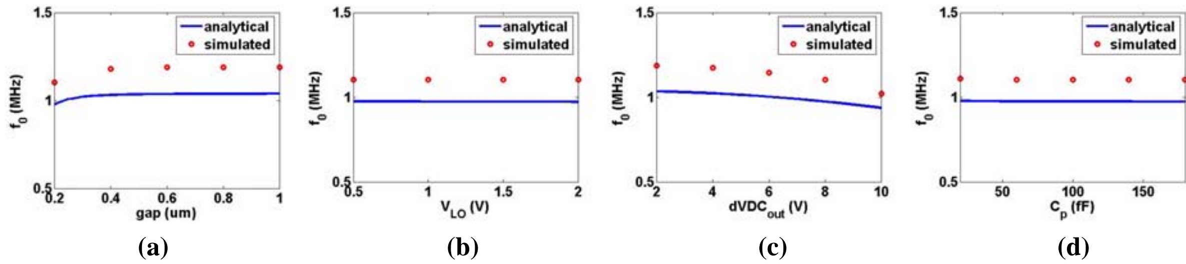

Figure 4-7 Resonant frequency **(a)** vs. gap for V_{LO} = 1 V, ΔV_{DCin} = 0 V, ΔV_{DCout} = 8 V and C_p = 150 fF, **(b)** vs. V_{LO} for gap = 0.2 μm, ΔV_{DCin} = 0 V, ΔV_{DCout} = 8 V and C_p = 150 fF, **(c)** vs. ΔV_{DCout} for gap = 0.2 μm, V_{LO} = 1 V, ΔV_{DCin} = 0 V, and C_p = 150 fF, **(d)** vs. C_p for gap = 0.2 μm, V_{LO} = 1 V, ΔV_{DCin} = 0 V, and ΔV_{DCout} = 8 V.

4.3.2 Conversion-Insertion Gain

Figure 4-8 below plots the conversion-insertion gain vs. gap (input and output gaps are equally sized), LO voltage amplitude, DC potential across the output transducer, and the load capacitance. It demonstrates a good match between the analytical and simulated data. Figure 4-8a proves that the transducer gap has the highest effect on the gain. However, it is not possible to employ gaps smaller than about 0.2 μm

for the 1 MHz mixer-filter, as the electrical spring constants (given in (2.46) of Chapter 2) exceed the mechanical spring value for the given voltages. Nevertheless, the loss can reduced below 10 dB using 0.2 μm gaps and <30 fF load capacitor as demonstrated in Figure 4-8d.

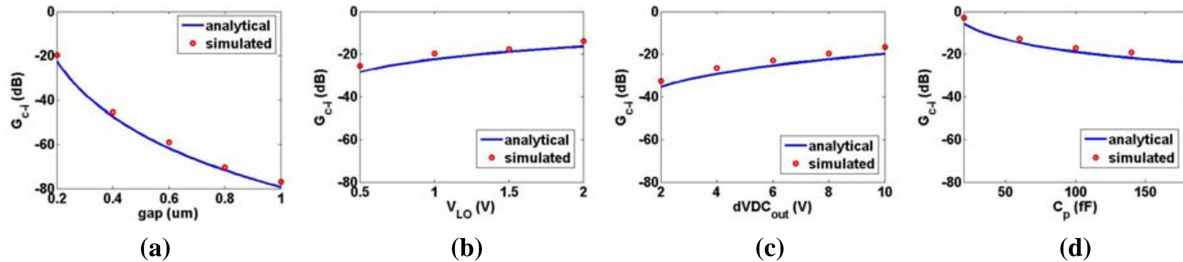

(a) (b) (c) (d)

Figure 4-8 Conversion-insertion gain **(a)** vs. gap for V_{LO} = 1 V, ΔV_{DCin} = 0 V, ΔV_{DCout} = 8 V and C_p = 150 fF, **(b)** vs. V_{LO} for gap = 0.2 μm, ΔV_{DCin} = 0 V, ΔV_{DCout} = 8 V and C_p = 150 fF, **(c)** vs. ΔV_{DCout} for gap = 0.2 μm, V_{LO} = 1 V, ΔV_{DCin} = 0 V, and C_p = 150 fF, **(d)** vs. C_p for gap = 0.2 μm, V_{LO} = 1 V, ΔV_{DCin} = 0 V, and ΔV_{DCout} = 8 V.

4.3.3 Noise Figure

The mixer-filter noise figure vs. input gap, LO voltage amplitude, and the RF source resistance are plotted below. The figures demonstrate a good match between the analytical and simulated data. The gap spacing is the most effective term as can been seen from Figure 4-9a. Taking the gap as 0.2 μm and the source resistance as 500 Ω gives a *NF* of ~55 dB, for the presented 1 MHz mixer-filter with a *Q* of 800. This value is still substantially higher than the typical *NF* of a Gilbert-type active mixer which is 10-20 dB [18].

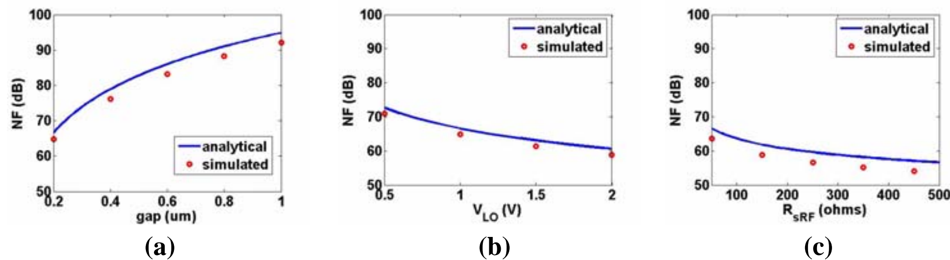

(a) (b) (c)

Figure 4-9 *NF* **(a)** vs. gap for V_{LO} = 1 V and R_{sRF} = 50 Ω, **(b)** vs. V_{LO} for gap = 0.2 μm and R_{sRF} = 50 Ω, **(c)** vs. R_{sRF} for gap = 0.2 μm and V_{LO} = 1 V.

4.3.4 Linearity

Figure 4-10 plots the calculated IIP3 voltage vs. the input gap and the DC potential across the input transducer. Here, we are able to present only the analytical results as the simulations did not run successfully due to convergence difficulties. Nevertheless, the IIP3 plots indicate practically impossible input voltages implying that the IM3 distortion is a not a concern for mixer-filters with practical gap sizes.

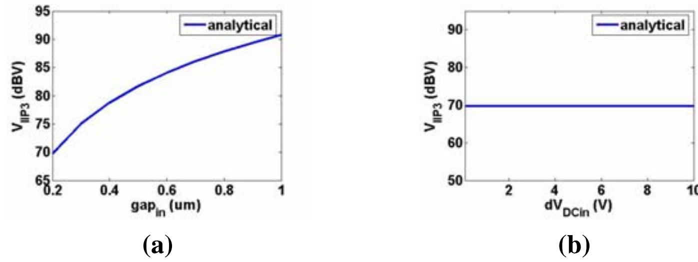

(a) **(b)**

Figure 4-10 IIP3 voltage **(a)** vs. input gap for f_0 = 1 MHz, f_{LO} = 100 MHz, V_{LO} = 1 V, and $\Delta V_{DCin} = \Delta V_{DCout}$ = 10 V, **(b)** vs. ΔV_{DCin} for f_0 = 1 MHz, f_{LO} = 100 MHz, V_{LO} = 1 V, gap_{in} = 0.2 μm, V_{LO} = 1 V, and $\Delta V_{DCout} = \Delta V_{DCin}$.

4.3.5 Discussion on Effective Damping

As we have already derived in Section 2.1.4 of Chapter 2, the effective damping coefficient for a mixer-filter is given by

$$b_{eff} = b_{mech} + b_{e,fb} = b_{mech} + \frac{\varepsilon_0^2 A_{in}^2 (R_{sRF} + R_{sLO})}{g_{in}^4}\left(\frac{\omega_{RF}}{4\omega_0} V_{LO}^2 + \Delta V_{DCin}{}^2\right). \qquad (4.1)$$

Inserting the measured Q_{eff} and ω_0 values (Q = 800, ω_0 = 1.05 MHz) together with the calculated k_{eff} (k_{eff} = 22.03 N/m) into (2.47) in Chapter 2 yields a b_{eff} of 4.2*10^{-9} N-s/m for the demonstrated mixer-filter. Using the measured dimensions listed in Table 4-1 and taking ω_{RF} = 100 MHz, ω_0 = 1.05 MHz, V_{LO} = 1.4 V, ΔV_{DCin} = 0 and $R_{sRF} = R_{sLO}$ = 50 Ω, the $b_{e,fb}$ is calculated as 1.25*10^{-15} N-s/m. Since $b_{eff} \gg b_{e,fb}$, we conclude that the mechanical damping dominates and $b_{eff} \approx b_{mech}$.

Now, finding out the gap size that sets $b_{mech} = b_{e,fb}$ may give some insight on the limits of the “mechanical damping dominates” assumption. Using the same values above, this gap is calculated as 18 nm,

which is much smaller than the typical values currently allowed by the CMOS-MEMS process. The assumption also holds valid for the performance trends demonstrated in Section 4.3.1-Section 4.3.4.

5 Conclusions

The potential use of CMOS-MEMS resonant mixer-filters in future single-chip multi-band radios have been discussed. An analytical model describing the mixer-filer operation has been developed and the design specifications that determine the device performance have been formulated. Some of the challenges in the mixer-filter design have been discussed and possible solutions have been proposed. A cantilever mixer-filter model has been built using NODAS and simulated in Cadence environment using SpectreRF simulator. An array of cantilever mixer-filters have been designed and fabricated.

The tested mixer-filter shows a center frequency of 1.05 MHz, bandwidth of 1.3 kHz and a conversion-insertion loss of 72 dB. The measured data is in good agreement with the simulated and analytical results. The simulated *NF* is 85 dB while the *IIP3* voltage is calculated as 88 dBV. The presented work is far from achieving acceptable performance in terms of gain and noise figure. Therefore, the design space has been explored by varying certain design parameters. It has been demonstrated that the loss can be reduced to acceptable levels by decreasing the transducer gaps and the load capacitance. The *NF* remains above 50 dB preventing the use of mixer-filters in the signal chain. However, the mixer-filter still holds the potential to be used in analog spectral sensors [8]. Besides, the *NF* may be reduced by two possible solutions: The gaps may be further reduced to the order of tens of nanometers by using innovative process and design techniques, which would necessitate stiffer resonators; or high amplification (>50 dB for 50 dB NF) may be provided before the mixer-filter using cascaded LNAs, which would boost the overall power consumption. This work has also shown that the mixer-filter naturally exhibits IM2 distortion, which may be rejected using differential LO topologies, and has a superior IM3 performance.

Bibliography

[1] B. Razavi, *RF Microelectronics*, Prentice Hall.

[2] L. Lin, C. T.-C. Nguyen, R. T. Howe, A. P. Pisano, "Microelectromechanical filters for signal processing," *Tech. Dig. IEEE MEMS Workshop*, Feb. 1992, pp. 226-231.

[3] C. T.-C. Nguyen, "Vibrating RF MEMS for next generation wireless applications," *Proc. IEEE Custom Integrated Circuits*, Orlando, Florida, Oct. 2004, pp. 257-264.

[4] G. K. Ho, R. Abdolvand, and F. Ayazi, "Through-support-coupled micromechanical filter array," *Proc. IEEE MEMS*, Maastricht, the Netherlands, Jan. 2004, pp. 769-772.

[5] S. Pourkamali, R. Abdolvand, G. K. Ho, and F. Ayazi, "Electrostatically Coupled Micromechanical Beam Filters," *Proc. IEEE MEMS*, Maastricht, the Netherlands, Jan. 2004, pp. 584-587.

[6] A. Wong, C. T.-C. Nguyen, "Micromechanical mixer-filters," *JMEMS,* vol. 13, no. 1, Feb. 2004, pp. 100.

[7] F. Chen, J. Brotz, U. Arslan, C.-C. Lo, T. Mukherjee, and G. K. Fedder, "CMOS-MEMS resonant RF mixer-filters," *Proc. IEEE MEMS*, Miami Beach, Florida, Jan.-Feb. 2005, pp. 24-7.

[8] T. Mukherjee, G. K. Fedder, H. Akyol, U. Arslan, J. Brotz, F. Chen, A. Jajoo, C. Lo, A. Oz, D. Ramachandran, and V. K. Saraf, "Reconfigurable MEMS-enabled RF circuits for spectrum sensing", *GOMACTech*, Las Vegas, Nevada, Apr. 2005.

[9] Q. Jing, *Modeling and simulation for desing of suspended MEMS*, Ph.D. Thesis, May 2003, Carnegie Mellon University, Pittsburgh, PA.

[10] G. K. Fedder, S. Santhanam, M. L. Reed, S. C. Eagle, D. F. Guillou, M. S.-C. Lu, and L. R. Carley, "Laminated high-aspect-ratio microstructures in a conventional CMOS process," *Sensors & Actuators*, Mar. 1997, pp. 103-110.

[11] G. K. Fedder, "CMOS-MEMS resonant mixer-filters," *Proc. IEEE IEDM*, Dec. 2005.

[12] J. Stillman, *CMOS-MEMS resonant mixer-filters*, M.S. Thesis, July 2003, Carnegie Mellon University, Pittsburgh, PA.

[13] J. Brotz, *Damping in CMOS-MEMS resonators*, M.S. Thesis, July 2004, Carnegie Mellon University, Pittsburgh, PA.

[14] A. T. Alastalo, M. Koskenvuori, H. Seppa, and J. Dekker, “A Micromechanical resonating RF mixer,” *34th European Microwave Conference*, Amsterdam, 2004.

[15] D. Ramachandran, *Design and characterization of a RF frequency-hopping filter*, M.S. Thesis, August 2004, Carnegie Mellon University, Pittsburgh, PA.

[16] R. Navid, J. R. Clark, M. Demirci, and C. T.-C. Nguyen, “Third-order intermodulation distortion in capacitively-driven cc-beam micromechanical resonators,” *Proc. IEEE MEMS*, Switzerland, Jan. 2001, pp. 228-231.

[17] K. Y. Yasamura, T. D. Stowe, E. M. Chow, T. Pfafman, T. W. Kenny, B. C. Stipe, and D. Rugar, “Quality factors in micron- and submicron-thick cantilevers,” *JMEMS,* vol. 9, no. 1, Mar. 2000, pp. 117-125.

[18] T. H. Lee, *The Design of CMOS Radio-Frequency Integrated Circuits*, Cambridge University Press.

[19] J. M. Tsai, G. K. Fedder, “Mechanical noise-limited CMOS-MEMS accelerometers,” *Proc. IEEE MEMS*, Miami Beach, Florida, Jan.-Feb. 2005, pp. 630-633.

[20] *SpectreRF User Guide*, Version 5.0, Cadence Design Systems, Inc., San Jose, CA, 2003.

[21] B. Razavi, “RF CMOS transceivers for cellular telephony,” *IEEE Communications Magazine*, Aug. 2003, pp. 144-149.

Appendix: Feedback Forces

At the input node, the interaction of the voltages ($v_{RF}(t)$, $v_{LO}(t)$, ΔV_{DCin}) with the resonator vibration generates an input current having components at mixed frequencies. The general expression for this input current is given by

$$i_{in}(t) = \frac{\partial}{\partial t}\{C_{in}[v_{RF}'(t) - v_{LO}'(t) + \Delta V_{DCin}]\} \tag{A.1}$$

where $v_{RF}'(t)$ and $v_{LO}'(t)$ are the voltages across the input gap at ω_{RF} and ω_{LO} respectively, as shown in Figure A-1 and the reader should note that these may differ from the source voltages, $v_{RF}(t)$ and $v_{LO}(t)$, due to loading.

Here, we focus only on the current components at ω_{RF}, ω_{LO} and ω_{IF} and try to understand how they alter the net IF force exerted on the resonator. The current term below generates the component at ω_{LO},

$$i_{in}(t) = \ldots - C_{0in}\frac{\partial v_{LO}'(t)}{\partial t} + \frac{\partial C_{in}}{\partial x}\left[x(t)\frac{\partial v_{RF}'(t)}{\partial t} + v_{RF}'(t)\frac{\partial x(t)}{\partial t}\right] + \ldots \tag{A.2}$$

where the displacement can be expressed as

$$x(t) = x\sin(\omega_{IF}t) \tag{A.3}$$

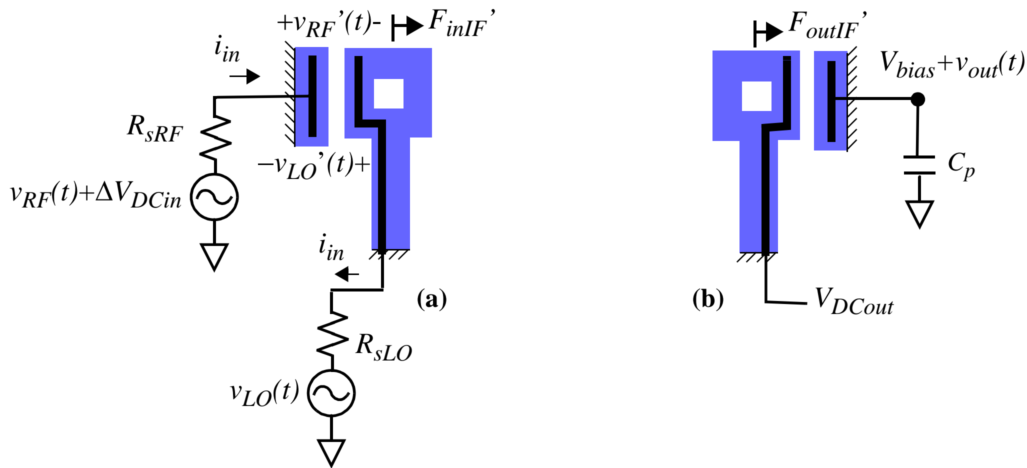

Figure A-1 Feedback forces at **(a)** input and **(b)** output nodes.

(Since the input force has multiple frequency components as shown in Table 2-1, vibrations will occur at those frequencies. However, we can assume that the primary vibration takes place at ω_{IF} as the displacements at high-frequencies are tiny. Besides, it is the IF component that give rise to input and output currents at ω_{RF}, ω_{LO} and ω_{IF}).

Inserting (A.3) together with the following

$$v_{RF}'(t) = V_{RF}' cos(\omega_{RF} t) \tag{A.4}$$

$$v_{LO}'(t) = V_{LO}' cos(\omega_{LO} t) \tag{A.5}$$

$$\frac{\partial C_{in}}{\partial x} = -\frac{C_{0in}}{g_{in}} \tag{A.6}$$

into (A.2) and using the basic trigonometric identities, the current term at ω_{LO}, i_{inLO}, is found to be:

$$i_{inLO}(t) = \frac{1}{2}\omega_{LO} C_{0in}\left[2V_{LO}' sin(\omega_{LO} t) - \left(\frac{x}{g_{in}}\right) V_{RF}' cos(\omega_{LO} t)\right]. \tag{A.7}$$

Using this, V_{LO}’ can be simply given by:

$$V_{LO}' = V_{LO} + I_{inLO}(R_{sRF} + R_{sLO}). \tag{A.8}$$

The RF voltage is typically much smaller than the LO voltage ($V_{RF} << V_{LO}$, thereby $V_{RF}' << V_{LO}'$) so that we can neglect the second term in (A.7). Thus, the effective network connecting the LO port to the RF includes two resistors (R_{sRF} and R_{sLO}) in series with a fixed capacitor (C_{0in}). For typical 50 Ω source resistors, the cut-off frequency of 10 GHz requires approximately a 150 fF capacitor, which is too large to be attainable even by using gaps in the range of tens of nanometres. Besides, we have to keep the input capacitance below the cut-off value to enable wideband operation. Thus, we can make the approximation $I_{inLO} \approx 0$, and thereby $V_{LO}' \approx V_{LO}$.

Now, we use the following term to get the input current at ω_{RF}

$$i_{in} = \ldots + C_{0in}\frac{\partial v_{RF}'(t)}{\partial t} - \frac{\partial C_{in}}{\partial x}\left(x(t)\frac{\partial v_{LO}(t)}{\partial t} + V_{LO}(t)\frac{\partial x(t)}{\partial t}\right) + \ldots. \tag{A.9}$$

Inserting (A.3), (A.4), (A.5) and (A.6), we get

$$i_{inRF}(t) = \frac{1}{2}\omega_{RF} C_{0in}\left[-2V_{RF}'\sin(\omega_{RF}t) + \left(\frac{x}{g_{in}}\right)V_{LO}\cos(\omega_{RF}t)\right]. \quad (A.10)$$

For small displacements (i.e. $x<<g_{in}$), and sufficiently small input capacitances as argued above, I_{inRF} can also be approximated as 0. However, for large displacements, the second term may not be negligible. In that case, we can express the input RF current as

$$i_{inRF}(t) = \frac{1}{2}\omega_{RF} C_{0in}\left(\frac{x}{g_{in}}\right)V_{LO}\cos(\omega_{RF}t). \quad (A.11)$$

Using the following relations

$$V_{RF}' = V_{RF} - I_{inRF}(R_{sRF} + R_{sLO}) \quad (A.12)$$

$$F_{inIF}(t) = \frac{\varepsilon_0 A_{in}}{2g_{in}^{\ 2}} V_{RF}V_{LO}\cos(\omega_{IF}t) \quad (A.13)$$

the force generated at the input transducer is found to be

$$\frac{\varepsilon_0 A_{in}}{2g_{in}^{\ 2}} V_{RF}'V_{LO}\cos(\omega_0 t) = F_{inIF}(t) - \frac{\varepsilon_0^2 A_{in}^2 \omega_{RF}(R_{sRF} + R_{sLO})}{4g_{in}^4} V_{LO}^2 x\cos(\omega_{IF}t). \quad (A.14)$$

Inserting

$$x\cos(\omega_{IF}t) = \frac{1}{\omega_{IF}}\frac{\partial x(t)}{\partial t} \quad (A.15)$$

we can rewrite (A.14) as

$$\frac{\varepsilon_0 A_{in}}{2g_{in}^{\ 2}} V_{RF}'V_{LO}\cos(\omega_{IF}t) = F_{inIF}(t) - \frac{\varepsilon_0^2 A_{in}^2 \omega_{RF}(R_{sRF} + R_{sLO})}{4g_{in}^4 \omega_{IF}} V_{LO}^2 \frac{\partial x(t)}{\partial t}. \quad (A.16)$$

In addition, the interaction of the input DC voltage with the displacement induces an input current at ω_{IF}, given by

$$i_{inIF}(t) = \Delta V_{DCin}\frac{\partial C_{in}}{\partial x}\frac{\partial x(t)}{\partial t}. \quad (A.17)$$

This current flows through the source resistors and converted to an IF voltage, v_{inIF}, given by:

$$v_{inIF}'(t) = -i_{inIF}(t)(R_{sRF} + R_{sLO}) = \frac{\varepsilon_0 A_{in}(R_{sRF} + R_{sLO})}{g_{in}^2}\Delta V_{DCin}\frac{\partial x(t)}{\partial t}. \quad (A.18)$$

The interaction of this voltage with the DC potential generates a feedback force, expressed as

$$F_{fb}(t) = \frac{1}{2}\frac{\partial C_{in}}{\partial x}(v_{inIF}'(t) + \Delta V_{DCin})^2 = \ldots - \frac{\varepsilon_0^2 A_{in}^2 (R_{sRF} + R_{sLO})}{g_{in}^4}\Delta V_{DCin}{}^2 \frac{\partial x(t)}{\partial t} + \ldots \quad \text{(A.19)}$$

Using (A.16), (A.19) and rearranging the terms, we find net force generated at the input port, F_{inIF}', as follows

$$F_{inIF}'(t) = F_{inIF}(t) - \frac{\varepsilon_0^2 A_{in}^2 (R_{sRF} + R_{sLO})}{g_{in}^4}\left(\frac{\omega_{RF}}{4\omega_{IF}} V_{LO}^2 + \Delta V_{DCin}{}^2\right)\frac{\partial x(t)}{\partial t}. \quad \text{(A.20)}$$

At the output node, an IF feedback force is generated by the interaction of the output voltage with the DC potential across the output capacitor (Figure A-1b). Thus, it is given by

$$F_{outIF}'(t) = \frac{1}{2}\frac{\partial C_{out}}{\partial x}[\Delta V_{DCout} - v_{out}(t)]^2 = \ldots - \frac{\varepsilon_0 A_{out}}{g_{out}^2}\Delta V_{DCout} v_{out}(t) + \ldots \quad \text{(A.21)}$$

Inserting

$$v_{out}(t) = \frac{\varepsilon_0 A_{out}}{g_{out}^2 (C_p + C_{0out})}\Delta V_{DCout} x(t) \quad \text{(A.22)}$$

we find the output feedback force as

$$F_{outIF}'(t) = -\frac{\varepsilon_0^2 A_{out}^2}{g_{out}^4 (C_p + C_{0out})}\Delta V_{DCout}{}^2 x(t) \quad \text{(A.23)}$$